Thermal versus elastic heterogeneity in high-resolution mantle circulation models with pyrolite composition: High plume excess temperatures in the lowermost mantle

B. S. A. Schuberth[1], H.-P. Bunge[1], G. Steinle-Neumann[2], C. Moder[1], and J. Oeser[1]

Abstract. We study a new class of high-resolution mantle circulation models and predict their corresponding elastic heterogeneity. Absolute temperatures are converted to seismic velocities using published thermodynamically self-consistent models of mantle mineralogy for a pyrolite composition. A grid spacing of ∼25 km globally allows us to explore mantle flow at earth-like convective vigor so that modeled temperature variations are consistent with the underlying mineralogy. We concentrate on isochemical convection and the relative importance of internal and bottom heating in order to isolate the thermal effects on elasticity. Models with a large temperature contrast on the order of 1000 K across the core-mantle boundary, corresponding to a substantial core heat loss of up to 12 TW, result in elastic structures that agree well with tomography for a number of quantitative measures: These include spectral power and histograms of heterogeneity as well as radial profiles of root-mean-square amplitudes. In particular, high plume excess temperatures of +1000–1500 K in the lowermost mantle lead to significant negative anomalies of shear wave velocity of up to −4%. These are comparable to strong velocity reductions mapped by seismic tomography in the prominent low-velocity regions of the lower mantle. We note that the inference of a large core heat flux is supported by a number of geophysical studies arguing for a substantial core contribution to the mantle energy budget. Additionally, we find significant differences between the characteristics of thermal heterogeneity and the characteristics of elastic heterogeneity in the transition zone due to phase transformations of upper mantle minerals. Our results underline the necessity to include mineral physics information in the geodynamic interpretation of tomographic models.

1. Introduction

Seismic tomography has advanced to a point where it provides considerable insight into the structure of the deep Earth. Particularly important for our understanding of deep Earth processes are two robust features of lower mantle heterogeneity (see Figure 1): One is a long wavelength fast seismic velocity anomaly concentrated into the circum-Pacific and regions under Asia [e.g., *Li and Romanowicz*, 1996; *Masters et al.*, 1996; *Grand et al.*, 1997; *van der Hilst et al.*, 1997; *Su and Dziewonski*, 1997; *Kennett et al.*, 1998; *Masters et al.*, 2000; *Ritsema and Van Heijst*, 2000; *Ritsema and van Heijst*, 2002; *Montelli et al.*, 2004, 2006]. It is now widely agreed upon by geodynamicists that this feature is associated with cold downwellings from past subduction driving a substantial part of the mantle general circulation [*Richards and Engebretson*, 1992; *Bunge et al.*, 1998; *Lithgow-Bertelloni and Richards*, 1998; *Becker and O'Connell*, 2001; *Conrad and Lithgow-Bertelloni*, 2002; *McNamara et al.*, 2002].

Less certain is the origin of another feature consisting of two pronounced low seismic velocity anomalies located beneath the Pacific and under Africa. Hot buoyant mantle from a strong thermal boundary layer at the core-mantle boundary (CMB) would provide a straightforward explanation for these anomalies. However, several studies argue that these regions are characterized by a different bulk composition from the surrounding mantle [*Ritsema et al.*, 1999; *Ishii and Tromp*, 1999, 2001; *van der Hilst and Karason*, 1999; *Wen et al.*, 2001; *Ni et al.*, 2002; *Ni and Helmberger*, 2003; *Ritsema and van Heijst*, 2002; *Deschamps and Trampert*, 2003; *Wang and Wen*, 2004]. Supporting evidence for this comes from probabilistic models of mantle heterogeneity [*Resovsky and Trampert*, 2003; *Trampert et al.*, 2004], and from seismic studies that simultaneously map the pattern of bulk sound and shear wave velocities [*Kennett et al.*, 1998; *Masters et al.*, 2000].

The complex character of the low seismic velocity anomalies has prompted geodynamicists to investigate the behavior of mantle flow with compositional variations [e.g., *Christensen and Hofmann*, 1994; *Davaille*, 1999; *Kellogg et al.*, 1999; *Tackley*, 2000, 2002], and to illuminate the dynamic consequences of a dense component in the deep mantle [*Hansen and Yuen*, 1989, 1994, 2000; *Montague and Kellogg*, 2000; *Davaille et al.*, 2002; *Stegman et al.*, 2002; *Jellinek and Manga*, 2004; *Nakagawa and Tackley*, 2004; *McNamara and Zhong*, 2004, 2005; *Farnetani and Samuel*, 2005].

Equally important for our understanding of these anomalies is the thermal state of the mantle, which is complicated by the simultaneous presence of mixed heating modes, i.e., by the effects of internal heating from radioactive decay and bottom heating from the core. The subadiabatic nature of the mantle geotherm away from thermal boundary layers is a direct consequence of internal heating, as noted early on by *Jeanloz and Morris* [1987], and there is growing consensus that the mantle geotherm departs by as much as 300–500

[1]Department of Earth and Environmental Sciences, Ludwig-Maximilians-Universität München, Germany

[2]Bayerisches Geoinstitut, University of Bayreuth, Germany

An edited version of this paper was published by AGU. Copyright (2009) American Geophysical Union.

K from the adiabat [*Matyska and Yuen*, 2000; *Bunge et al.*, 2001; *Monnereau and Yuen*, 2002; *Sleep*, 2003].

Mantle non-adiabaticity points to a strong thermal gradient and a correspondingly high heat flux across the CMB [*Bunge*, 2005; *Mittelstaedt and Tackley*, 2006; *Zhong*, 2006; *Lay*, 2008], as large as 30 percent (∼10 TW) of the total mantle heat loss. Thus, it is likely that bottom heating plays a more prominent role in the mantle general circulation than what is commonly inferred from arguments based on the dynamic topography over hotspots [*Davies*, 1988; *Sleep*, 1990]. It is therefore important to study the nature of heterogeneity in global mantle circulation models (MCM) when strong core heating is present. Of course, mantle heterogeneity modeled by geodynamicists must be compared to the seismic properties mapped by tomography. Both are related through the material properties of mantle mineralogy. In this respect, however, interpretations have remained limited as the trade-offs between thermal and chemical effects have not allowed an unequivocal identification of the cause of heterogeneities both for the upper [*Cammarano et al.*, 2003] and the lower mantle [*Deschamps and Trampert*, 2004; *Mattern et al.*, 2005; *Matas et al.*, 2007].

In this study, we test in a forward modeling approach whether strong core heating results in seismic heterogeneity compatible to observations in spectral characteristics and magnitude. To keep things simple, and to isolate the effects of core heating, we focus our attention on isochemical global mantle circulation. The pyrolite model [*Ringwood*, 1975; *Irifune*, 1987] is consistent with this choice.

We start this paper with a brief description of the computational methods and parameters employed. We next investigate the thermal heterogeneity of mantle flow with a substantial amount of core heat flux (as much as 12 TW), and isolate the effects of core heating from variations in the radial viscosity profile through simple end-member models. We explore the influence of thermal structure on corresponding heterogeneities in shear (v_s) and compressional (v_p) wave velocity, which we compare to tomographic models directly and with statistical measures. For the conversion of temperatures into elastic parameters we take advantage of progress in mineral physics and use two recently published thermodynamic models of mantle mineralogy [*Piazzoni et al.*, 2007; *Stixrude and Lithgow-Bertelloni*, 2007], coupled to a model of shear moduli [*Stixrude and Lithgow-Bertelloni*, 2005]. In both models, stable phase assemblages in the CFMAS (CaO – FeO – MgO – Al_2O_3 – SiO_2) system are computed by Gibbs Free Energy minimization. We refer to these models hereafter as PSBD and SLB, respectively.

In the analysis of seismic properties and their relation to temperature via a mantle mineralogy model one needs to pay special attention to the vigor of convection, as one must ensure that modeled temperature variations are consistent with temperature variations assumed in the underlying mineralogy. To this end, we capitalize on growing computational resources and employ new global mantle circulation models at very high numerical resolution. This allows us to approach for the first time the vigorous regime of global mantle flow and to construct its corresponding elastic structure. Our models do not preclude the existence of chemical variations, but they suggest that the large-scale elastic heterogeneity of the mantle can be understood in terms of isochemical whole mantle circulation with strong hot upwellings from the CMB.

2. Computational Methods, Boundary and Initial Conditions

We compute global mantle flow with the parallel finite element code TERRA, which has been benchmarked [*Bunge*, 1996] and described in detail before [*Bunge and Baumgardner*, 1995; *Bunge et al.*, 1996, 1997]. The code solves the momentum and energy balance at infinite Prandtl number (no inertial forces) in a spherical shell, with the inner radius being that of the outer core and the outer radius corresponding to Earth's surface. The computational domain is discretized with a mesh derived from the regular icosahedron, providing almost equidistant grid spacing throughout the mantle. A key difference to earlier studies [e.g., *Bunge et al.*, 2002] is the very high resolution of the mesh with more than 80 million finite elements. The models are implemented on 128 cores of a topical compute cluster dedicated to large-scale geophysical modeling [*Oeser et al.*, 2006]. The horizontal resolution is 30 km at the outer surface, and decreases to half that value at the CMB, while a uniform radial grid spacing of 25 km is applied throughout the shell. This fine discretization allows us to explore large-scale mantle flow at earth-like convective vigor and to employ a thermal Rayleigh number of 10^9 based on internal heating; that is, we are able to resolve a characteristic thermal boundary layer thickness on the order of 100 km, comparable to that of oceanic lithosphere.

Our circulation models incorporate mantle compressibility effects in form of the anelastic liquid approximation [*Jarvis and McKenzie*, 1980; *Glatzmaier*, 1988], and the radial variation of state variables is represented through a Murnaghan equation of state [*Murnaghan*, 1951] with parameter values identical to [*Bunge et al.*, 2002]. We apply a thermal conductivity of 3.0 $\mathrm{W\,m^{-1}\,K^{-1}}$ and an internal heating rate of 6.0×10^{-12} $\mathrm{W\,kg^{-1}}$ throughout this study, roughly the chondritic value [*Urey*, 1956]. Thermal boundary conditions are constant temperature at the surface (300 K) and the CMB. The latter is chosen such as to produce models with weak or strong core heat flux (see section 2.1). Mechanical boundary conditions are always free-slip (no shear-stress) at the CMB, while velocities are specified at the surface according to a widely adopted plate motion history model [*Lithgow-Bertelloni and Richards*, 1998] that spans the past 120 million years (Ma). Meteorologists refer to this approach as *sequential* data-assimilation [see *Talagrand*, 1997, for a review].

The high numerical resolution in our models requires an interpolation of all plate boundaries between successive plate stages, similar to *Steinberger* [2000], to avoid unrealistic separation of slab fragments. The interpolation is performed at 1 Ma intervals and involves geometric, but no geologic considerations. For this, we created a set of 120 plate configurations based on the eleven plate stages of *Lithgow-Bertelloni and Richards* [1998] while keeping their corresponding set of eleven Euler poles.

The large convective vigor in our models has the effect that the RMS surface velocity obtained from an independent set of free convection simulations (with no imposed plate motion) approaches earth-like values (about 5 cm/yr). This remarkable observation allows us to keep time identical to Earth time in all simulations, and to avoid scaling the assimilated plate velocities to lower values.

A general problem in mantle circulation modeling is the choice of an initial condition. This choice is rather arbitrary, as the structure of the mantle sometime in the past is principally unknown. Here, we follow the philosophy of *Bunge et al.* [1998, 2002] and approximate the unknown initial conditions of mid-Cretaceous mantle heterogeneity by running our models with global plate configurations fixed to the oldest available reconstructions at 120 Ma ago until they reach a thermal quasi steady-state.

Finally, the temperature field of the MCMs is post-processed and mapped to seismic velocities using the two thermodynamically self-consistent models of mantle mineralogy, PSBD and SLB, mentioned in section 1. In this simple approach, phase transitions of upper mantle minerals are therefore incorporated in our elastic models, even though

their dynamic effects on the flow are not included in the calculations.

2.1. Model Setup

We focus on four mantle circulation models (M1–M4) and explore variations in the amount of bottom heating and the radial viscosity structure, while keeping all other model parameters constant (see Table 1). Our radial viscosity profiles account for three distinct layers (which we identify with the lithosphere, the upper and the lower mantle, respectively) separated at 100 km and 660 km depth. These are inferred from geoid [e.g., *Hager and Richards*, 1989] and post glacial rebound studies [*Paulson et al.*, 2007] as a first-order rheological stratification of Earth's mantle. Each model includes a relatively strong lithosphere, where the viscosity is 10^{23} Pa s. The upper mantle viscosity in model M1 is 10^{21} Pa s, the Haskell value [see *Mitrovica*, 1996], and increases by a factor of 100 in the lower mantle. We ease the notation and index our model viscosities to the Haskell value, which we denote as "1". Thus, the viscosity profile of M1 is 100, 1, 100 for the lithosphere, the upper and the lower mantle, respectively. A modest CMB heat flux of 1.5 TW (around 5% of the total surface heat flow) is accomplished by setting the CMB temperature to 2900 K.

The viscosity profile of M2 is identical to M1, but we impose a much higher core heat flux of 12 TW (roughly 35% of the surface heat flow) by setting the CMB temperature to 4200 K. This makes M1 and M2 end-members in terms of core heating with Urey numbers (the ratio of internal heating to total surface heat loss) of 0.95 and 0.65, respectively. M3, to which we ascribe a viscosity profile of 100, 0.5, 100, in effect explores the influence of a mechanically weaker upper mantle (relative to M1 and M2) and a correspondingly higher upper/lower mantle viscosity jump. A core heat flow of 9 TW (roughly 25% of the surface heat flow) is accomplished by setting the CMB temperature to 4000 K. M4 (with a profile of 100, 0.5, 50) reduces the overall mantle viscosity relative to M1, and moves the upper/lower mantle viscosity jump to 450 km depth. The depth and magnitude of the viscosity contrast between upper and lower mantle is not well known. We therefore chose to test a shallower depth in combination with the reduced overall viscosity in M4. A core heat flux of 10 TW (around 30% of the surface value) results from a CMB temperature of 3500 K in this case. Note that M4 produces a heat flow comparable to M2 and M3 despite its lower CMB temperature. This is a consequence of the reduced viscosity and the correspondingly more vigorous convection in this model. Together, M1–M4 span a reasonable range of mantle viscosity and core heat flux values, which are summarized in Table 2.

3. Results

3.1. Lateral Thermal Heterogeneity

Figure 2 shows three-dimensional (3-D) views of the temperature distribution in M2. The four view angles are centered on the Atlantic, the Indian Ocean, and the western and eastern Pacific, respectively. The earth-like convective vigor produces a narrow, upper thermal boundary layer with a thickness of about 100 km, and correspondingly thin and elongated downwellings in regions of present day plate convergence (e.g., under the Marianna and Izu-Bonin subduction systems, the Sumatra and Tonga-Kermadec trench). Remnants of the Tethyan subduction are visible in a broad upper and mid-mantle region under Eurasia. Subduction of the old Farallon plate is evident in the deeper mantle under eastern North America and under South America. In the lowermost mantle, prominent hot upwellings are located in the southeast Pacific and under southern Africa up to Europe and Iceland (see top panels in Fig. 2). While the upwellings are consistent with the dynamics of flow with strong core heat flux, their morphology and location are entirely due to the model initialization, since the available plate motion history is too short to affect the pattern of deep mantle heterogeneity (see *Bunge et al.* [2002] for a discussion, and *Torsvik et al.* [2008] for efforts to extend plate motion histories to longer time periods in the past).

A remarkable feature is the spontaneous emergence of the asthenosphere as a region of relatively uniform temperature with much less thermal heterogeneity (the thin, almost white band in the upper mantle in Fig. 2, bottom panels). Due to the lower viscosity in this layer, material flows laterally over considerable distance (see thermal upwelling under the East Pacific Rise which feeds a broad region of hot asthenosphere in the equatorial Pacific), and as a result thermal variations are effectively equilibrated. This agrees well with petrological studies, which infer only minor melting temperature variations beneath the global mid-ocean ridge system [*McKenzie and Bickle*, 1988; *Presnall and Gudfinnsson*, 2008].

Horizontal sections through M1 and M2 are shown in Figure 3. Columns one and two (from left to right) illustrate how thermal structure varies between models with high and low core heat flux. Starting from the top, at 100 km depth, cold downwellings dominate the thermal heterogeneity pattern, as noted before. Continental regions and the oldest parts of the oceans are also colder than average, while hot material beneath oceanic regions follows the global distribution of spreading centers. Slabs control the thermal structure also at 340 km depth. Deeper down at 800 km depth, prominent cold downwellings are located around the Pacific, but their position differs from shallower depth levels because they reflect earlier stages of plate subduction (e.g., cold material associated with subduction of the Farallon plate east of North America's West Coast, and remnants of the Tethys Ocean as a distinct cold feature beneath Africa, Arabia and India). A hot thermal anomaly in M2 is located in the southeast Pacific.

There is little overall change in the mid mantle, at 1450 km depth, except for the location of downwellings. Here, the Farallon slab lies east of North America, and remnants of subduction exist under central America. The feature with the largest thermal amplitude is a group of downwelling slabs corresponding to the broad collision of India and Eurasia. Cold material exists also under the north Pacific, which can be traced back to the convergence of the North American and Kula plate 50–70 Ma ago according to the reconstructions. Significant differences between M1 and M2 appear between 2000 km and the CMB. M2 is dominated by prominent hot upwellings under the South Pacific Ocean and (to a lesser extend) in the Indian Ocean, while cold material spreads laterally in both models as it approaches the lowermost mantle and the CMB. Near the CMB at 2800 km depth, hot upwellings in M2 give rise to large lateral temperature variations, reaching maximum positive values of up to +1500 K (see also Figure 6), while in model M1 there are much smaller variations on the order of +200–250 K.

3.2. Radial Profiles of Temperature, v_s, v_p and Density

Figure 4a shows the averaged temperature profiles of models M1–M4 and a 1750 K reference adiabat. As expected, all geotherms are subadiabatic due to internal heating and are up to 350–550 K lower than the reference adiabat in the lowermost mantle (2500–2700 km depth).

Density profiles for M2 obtained in combination with the mineralogical models PSBD and SLB are shown in Figure 4b, together with the density profiles of PREM and AK135M [*Dziewonski and Anderson*, 1981; *Kennett et al.*, 1995]. We

focus on M2 in this and the remaining subfigures, because the variability of 1-D profiles between the MCMs is small. Both mineral physics models predict similar densities in the upper 1200 km of the mantle. They also provide rather good estimates of depth and magnitude of the density jumps across the discontinuities, as well as a reasonable gradient in the transition zone.

Figure 4c shows the v_s profiles inferred from M2. Both profiles run virtually parallel in the transition zone and the lower mantle. However, model SLB gives S-wave velocities about 1.5–2% lower than model PSBD, the latter being in reasonable agreement with the seismic reference profiles. The gradient of v_s in the lower mantle is larger than observed for both models of mantle mineralogy. The predicted P-wave profiles (Fig.4d) are also parallel in most of the mantle, but show exactly opposite characteristics to v_s. Model SLB now gives higher v_p values than PSBD and their gradients are again larger than for the seismic models. The fact that both mineral physics models predict parallel offset profiles in v_s and in v_p can be traced back to differences in their databases and demonstrates the need to reduce uncertainties in experimental values.

For both P- and S-wave velocities, the depth of the 410 km discontinuity is overpredicted using either of the mineralogical models. Together with the low values of the seismic velocities in the upper mantle, and assuming that pyrolite is a reasonable estimate of mantle composition, this indicates that the absolute temperatures may be overestimated.

Changing the average temperature profile may improve the fit to the seismic observations. We tested this in that we lowered the geotherm of M2 by 500 K resulting in a temperature profile with 1250 K footing temperature, but no change in slope compared to the original profile. A geotherm with footing temperature of around 1250 K (roughly 1000 °C) is unlikely in the Earth. Typical estimates derived from melting temperatures of basalts at mid-ocean ridges yield values of around 1350 °C or roughly 1600–1650 K, which is much closer to our original geotherm. The v_s profile from the artificially lowered geotherm using model SLB falls closer to the values of PREM and AK135M, but is still too low by 0.3–0.5% in the lower mantle. At the same time, density and v_p are larger than the seismic reference values. We note that the upper mantle temperature in our simulations depends mostly on the viscosity structure of the lithosphere (i.e., both absolute values and thickness), which leaves room for lowering the overall temperatures in future simulations and to bring our predicted 1-D profiles closer to observations. However, since this study focuses on 3-D variations we do not intend to fit seismic reference profiles.

3.3. Thermal vs. Elastic 3-D Heterogeneity

We return to Figure 3 where relative variations in S- and P-wave velocity derived from model M2 are shown in columns three and four. The elastic heterogeneity is inferred by converting absolute model temperatures to absolute values of S- and P-wave velocity using the mineralogical model SLB for a pyrolite composition. Relative variations are then computed with respect to the mean seismic velocity at each depth. The main effect of the conversion is to amplify heterogeneity in the uppermost mantle, while there is a trend toward less heterogeneity with depth. Note that shear velocity variations are much stronger throughout the mantle than variations in compressional velocity.

3.3.1. Spectral Characteristics

Spectral heterogeneity maps (SHM) [*Jordan et al.*, 1993], which are contour plots of spectral amplitude $vs.$ depth, for all four MCMs are shown in Figure 5. In the following, we consider temperatures together with shear wave velocities based on the mineralogical model SLB. Radial profiles of the root-mean-square (RMS) power of the spherical harmonics expansion are also shown. Spectral power σ_l per degree l is computed at each depth level and for spherical harmonics degrees $l = 1, \ldots, 20$ by [*Dahlen and Tromp*, 1998, B.8]

$$\sigma_l = \sqrt{\frac{1}{2l+1}\left[a_{l0}^2 + \sum_{m=1}^{l}(a_{lm}^2 + b_{lm}^2)\right]}, \quad (1)$$

where a_{lm} and b_{lm} are the coefficients of the expansion and the RMS power is given by:

$$\delta\hat{v} = \sqrt{\frac{1}{\sqrt{4\pi}}\sum_{l=1}^{l_{max}}(2l+1)\sigma_l^2}\,. \quad (2)$$

Spectral power of thermal heterogeneity (Fig. 5a–d) is concentrated in the upper and lower thermal boundary layers of all MCMs, i.e., in the lithosphere and in the lowermost mantle. Thermal variations in the lithosphere exist on a broad range of spatial scales as indicated by strong spectral power in all spherical harmonic degrees. In the low-viscosity upper mantle, by comparison, there is much less thermal heterogeneity. The strength of heterogeneity increases again at the top of the lower mantle due to the higher viscosity there. Starting at around 750 km depth, pronounced heterogeneity at the largest length scale (spherical harmonic degree two) exists in all models, with a further increase in heterogeneity amplitude from the mid mantle (1500 km) downward. This low order pattern is due to the dominant long wavelength planform of the oldest stages of assimilated plate motion history from 80 to 120 Ma ago, and reflects the combined effects of plate motion and viscosity stratification [*Bunge and Richards*, 1996]. In the deepest mantle, and approaching the lower thermal boundary layer, heterogeneity can also be found in higher degrees. Note that the weak mid mantle heterogeneity in M4 (Fig. 5d) reflects the lower viscosities in this model. The overall distribution of heterogeneity, with maxima near the top and bottom thermal boundary layers, is also reflected in the radial profiles of RMS spectral power in all four MCMs.

The spectral heterogeneity maps for v_s, displayed in Figures 5e–h, look rather different compared to those of temperature, which reveals the strong effects of mantle mineralogy. They only show similarities in the overall characteristics (strong heterogeneity in the lithosphere and the lowermost mantle, dominated by long wavelength structure). The biggest difference in spectral power between v_s and thermal variations exists in the upper mantle, where narrow bands of spectral power up to degree 20 are visible for v_s. These correspond to the major phase transformations in the transition zone at 410 km, 520 km and 660 km depth. Variations in the amount of CMB heat flow influence the power distribution less than the differences in radial viscosity profiles (compare e.g., Figs. 5e,f and h), as the radial viscosity structure primarily controls the speed of flow and therefore the depth of subducted material. A higher CMB heat flux instead increases the amplitude of lower mantle heterogeneity, e.g., more heterogeneity is present in the lowermost mantle in model M2 compared to M1 and also in higher degrees.

The difference in spectral heterogeneity between temperature and shear wave velocity in the upper mantle can be explained by the increased sensitivity of shear wave velocity to temperature at the upper mantle discontinuities. This sensitivity is the result of two combined effects: On the one hand temperature directly influences the elastic properties of a fixed phase assemblage. On the other hand, temperature also affects the stable phase assemblage, which in turn

strongly changes the elastic properties of the bulk rock [*Ricard et al.*, 2005; *Stixrude and Lithgow-Bertelloni*, 2007]. The latter effect is most significant in the upper mantle, leading to the fine scale heterogeneity observed in v_s in the transition zone.

The change in pattern between thermal and elastic spectral heterogeneity suggests caution in the geodynamic interpretation of tomographic models (v_s or v_p). For example, from the spectral characteristics of v_s in Figures 5e–h one may argue for a change in the convective style between the upper and lower mantle. The underlying thermal variations in the geodynamic models, however, show an increase in the power of heterogeneity from the upper to the lower mantle, opposite to what is seen in the elastic parameters. As noted before, this is the result of an increase in viscosity at the upper mantle/lower mantle boundary, which however, does not inhibit mass exchange.

3.3.2. Amplitude Distributions of 3-D Heterogeneity

Histograms of variations in temperature and shear wave velocity are shown in Figure 6. We contour the total number of model grid points at any given depth (y-axis) as a function of their temperature or shear wave anomaly (x-axis) relative to the horizontal mean. We consider thermal heterogeneity first (Figs. 6a–d) and note that the largest number of model grid points in each depth has temperatures near the mean radial value, as expected for vigorous convection. In other words, thermal anomalies are small nearly everywhere, as heat transport is dominated by advection outside the thermal boundary layers. All histograms reveal maximum cold thermal anomalies (slabs) on the order of −1000–1500 K at all depth levels, which correspond to the temperature drop across the upper thermal boundary layer, as expected. The minor fluctuations with depth reveal transient features in the subduction history; that is, these changes can be attributed to variations in the amount of subducted slab material at different plate tectonic stages.

The most pronounced difference between the MCMs occurs for hot anomalies, i.e., plumes rising from the thermal boundary layer above the CMB. Model M1 with a weak lower thermal boundary layer and a correspondingly low core heat flux is characterized by low amplitude positive temperature variations with magnitudes less than +500 K. In contrast to that, the MCMs with high CMB heat flow (M2–M4) show large positive values in the lower mantle and a strong decrease of plume excess temperatures as the material rises adiabatically in the otherwise subadiabatic mantle. In these models, hot (positive dT) anomalies are reduced from around +1000–1500 K at the CMB to +200–300 K in the upper mantle.

All histograms are asymmetric with respect to their bounds in most of the depth levels. Moreover, they show a strong increase in variance and spread with depth in the lower mantle, except for M1. Thermal heterogeneity of all models is characterized by substantial negative skew in the upper mantle outside the lithosphere, and only models with high CMB flux show a gradual change to positive skewness in the lowermost mantle and a nearly bi-modal distribution, there.

Similar to the spectral heterogeneity maps, the histograms for shear wave velocity in Figures 6e–h differ considerably from those of temperature. Most of the difference is due to the general decrease in sensitivity of shear wave velocity to temperature with depth [*Trampert et al.*, 2001; *Cammarano et al.*, 2003; *Goes et al.*, 2004; *Stixrude and Lithgow-Bertelloni*, 2007]. This can be seen, for example, when comparing maximum positive temperature variations in Figure 6b to the corresponding shear velocity anomalies in Figure 6f. While the hot temperature anomalies increase strongly with depth in the lower mantle, their respective S-wave perturbations remain nearly constant. In consequence, the largest spread of S-wave perturbations is located in the upper mantle exceeding values of 8% on the positive side. Strong variations in the transition zone directly show the influence of phase changes and the corresponding changes in elastic parameters.

Moreover, the comparison of thermal and seismic heterogeneity reveals the non-linearity introduced through the mineralogical model, which has also been observed by *Goes et al.* [2004]. Positive temperature variations lead to larger variations in v_s than negative variations (e.g., for model M2: $\frac{dlnv_s}{dT} = -5.1 \times 10^{-5}$ at ∼2500 K vs. -4.0×10^{-5} K^{-1} at ∼1500 K in the upper part of the lower mantle; and -2.9×10^{-5} at ∼3000 K vs. -2.5×10^{-5} K^{-1} at ∼2000 K in the lowermost mantle, respectively). This non-linearity results in a modification of the spread and asymmetry in the histograms. Model M2 shows the strongest asymmetry in the lowermost mantle with values of more than −4% compared to +2% on the positive side. Especially the large slow values exceeding −4% are remarkable. In contrast to that, the small positive thermal variations in model M1 result in much smaller negative v_s perturbations of around −1%. This marks the significant difference to models with strong core heating. In addition, the latter are characterized by a change from positive skewness in the upper part of the lower mantle to negative skewness near the CMB. Furthermore, they have a peak at fast seismic velocities in the lowermost mantle and show a strong increase of variance with depth.

4. Comparison of Modeled Heterogeneity to Tomography

4.1. Comparison of Spectral Characteristics

Figure 7 shows the spectral characteristics of the four tomographic models from Figure 1. In all models, heterogeneity is concentrated in the lithosphere, the upper mantle and the lowermost lower mantle. The significant power in higher degrees close to the surface and the CMB indicates considerable small scale heterogeneity. Note also that model PRI-S05 was built using body wave data only [*Montelli et al.*, 2006], which may be the reason for the lower spectral heterogeneity in the lithosphere compared to the other models. All spectra are "red" and generally show a strong degree two signal in most of the lower mantle (S20RTS, TX2007 and HMSL-S06). Heterogeneity is weakest in the mid mantle and all models show a change in spectral power from the transition zone into the lower mantle.

Our isochemical mantle circulation models are in good agreement with these characteristics, which also show a concentration of heterogeneity close to thermal boundary layers and a red spectrum. The latter results from the combination of large-scale plate motion and a high viscosity lower mantle [*Bunge and Richards*, 1996]. The MCMs also display a change in the spectra of elastic heterogeneity from the upper to the lower mantle. As discussed in section 3.3.1 this is due to the mineralogical properties of the mantle.

4.2. Comparison of Amplitudes

In Figure 8, we plot histograms of the tomographic S-wave models. Note that they show considerable differences among each other, especially in the spread of amplitudes. Models S20RTS and TX2007 have much smaller amplitudes in almost all depth levels compared to models HMSL-S06 and PRI-S05, which may reflect differences in tomographic resolution due to different inversion procedures or data sets used. The variability of the maxima in the lower mantle, which however is less than in our MCMs, may be a combination of transient geodynamic features, as well as artifacts

from the inversion. In all histograms, the peak deviates from the mean value in certain depths, most strongly so in the lowermost mantle where all models show a shift to positive variations. Furthermore, the variance increases close to the CMB. Interestingly, extreme values are asymmetric in the lowermost mantle, with negative v_s perturbations of up to -4% compared to $+2\%$ on the positive side (especially in models HMSL-S06 and PRI-S05). At the same time, the histograms have negative skewness there, as opposed to the positive skewness in the upper part of the lower mantle, a feature that has been noted also by *Yanagisawa and Hamano* [1999] for other S-wave velocity models. Similar to all histograms is that the largest perturbations occur in the lithosphere and upper mantle which is consistent with the high spectral power observed in this depth range.

The geodynamic models with strong core heating show the same marked asymmetry in the lowermost mantle with negative v_s anomalies of up to -4%, while the values of around -1% in model M1 are much lower than observed. Moreover, they also display a change in skewness from positive to negative throughout the lower mantle and a peak at positive values close to the CMB supporting the notion that the mantle is heated substantially from below. Furthermore, the skewness pattern indicates that thermal structure in the mantle is dominated by cold downwellings (i.e., slabs) down to 1500 km, and very hot active upwellings at greater depths. *Yanagisawa and Hamano* [1999] have argued along similar lines based on 2-D convection simulations in a Cartesian setup and a direct comparison of resulting temperatures to tomographic shear wave models. The results in Figure 6 show that this conclusion is largely independent of the details of the radial viscosity structure.

One robust property inferred from tomography is an increase in the RMS amplitude of seismic heterogeneity below 2000 km depth, often taken as an indication for deep mantle chemical heterogeneity. In Figure 9a and 9b we plot RMS profiles of the four tomographic S-wave models and six additional P-wave models, all of which show the largest RMS amplitudes in the upper 200 km of the mantle and a gradual increase from a minimum in the mid-mantle to values of around 1% for v_s and 0.3–0.5% for v_p close to the CMB. For ease of comparison to our MCMs, we construct upper and lower bounds from the tomography profiles by taking the maximum and minimum RMS values of all tomographic models in each depth (black dashed and dash-dotted lines, respectively in Figs. 9c and 9d). In most of the mantle, the geodynamic RMS profiles of v_s and v_p lie within these bounds. Only model M2 gives larger values in the lowermost mantle for both seismic velocities. At the transition zone discontinuities, the RMS amplitudes of the MCMs show strong variations and large values as a consequence of the complex sensitivity of v_s to temperature, as noted before. Lower values and less variation in the tomographic models may be related to vertical smearing of heterogeneity from the transition zone into the uppermost lower mantle, where the geodynamic models show values at the lower bound.

5. Discussion

We have investigated the thermal and elastic structure of high-resolution mantle circulation models and find that whole mantle flow with strong core heating is compatible with a variety of quantitative measures inferred from tomography: histograms, RMS amplitudes, and spectral power of variations in shear wave velocity. In particular, the hot lower mantle thermal anomalies on the order of 1000 K and the corresponding reduction in shear wave velocity of up to -4%, which we infer using published models of mantle mineralogy [*Piazzoni et al.*, 2007; *Stixrude and Lithgow-Bertelloni*, 2005, 2007], agrees remarkably well with shear wave anomalies mapped in low seismic velocity regions of the deeper mantle (see histograms in Figures 6e–h and 8). Apart from the isochemical, pyrolitic nature of our models, we have made three basic assumptions in the construction of global geodynamic mantle heterogeneity: 1) a large-scale flow structure related to past plate motion, 2) a radial viscosity profile that agrees with post-glacial rebound and geoid observations, and 3) a significant vertical temperature change across the CMB of $\sim$1000 K corresponding to a large core heat flow of 9–12 TW.

5.1. Amplitudes of Seismic Heterogeneity and Plume Excess Temperature

While the first two assumptions are reasonably well agreed upon by geodynamicists, the third assumption requires careful consideration, being promoted, as it is, by a number of recent studies: *van der Hilst et al.* [2007], for example, find a CMB temperature of 3950$\pm$200 K from inverse scattering of core-reflected shear waves (ScS). CMB temperature values between 3500 and 4000 K and a large jump of 1000–1500 K across D" are also suggested by *Steinberger and Holme* [2008], who fit models of instantaneous mantle flow, which are based on density variations derived from tomographic shear wave models, to the geoid and observations of CMB excess ellipticity and topography. High-pressure experiments on the melting temperature of iron alloys also point to a high CMB temperature of 4000$\pm$200 K and a correspondingly large temperature drop on the order of 1000 K at the base of the lower mantle as reviewed by *Boehler* [2000]. These results are further supported by first-principle calculations of the elastic parameters and melting curve of iron under core conditions. When combined with seismic constraints the material simulations place estimates of the inner-core boundary (ICB) temperature at 5400–5700 K [*Steinle-Neumann et al.*, 2001; *Alfè et al.*, 2002]. Correcting for the adiabatic gradient through the outer core this translates to a CMB temperature of about 4000 K and a high excess temperature of deep mantle upwellings [*Alfè et al.*, 2007].

The near surface excess temperature of mantle upwellings by comparison is rather small, ranging between +200 and +300 K [*Schilling*, 1991]. The much larger excess temperatures in the deeper mantle, however, can be gleaned from two thermodynamic considerations: First, as noted before, internal heating in combination with the slow overturn of the mantle lowers the geotherm by 300–500 K compared to an adiabat [*Jeanloz and Morris*, 1987; *Matyska and Yuen*, 2000; *Bunge et al.*, 2001; *Monnereau and Yuen*, 2002; *Sleep*, 2003; *Mattern et al.*, 2005]. The temperature distribution in plumes instead is nearly adiabatic, as they rise relatively quickly through the mantle, on a time scale on the order of 100 Ma. The net effect is a systematic increase of plume excess temperature by about 300 K as one moves deeper into the mantle [*Bunge*, 2005]. The second consideration follows from the adiabatic gradient being proportional to temperature. This implies a steeper thermal gradient in plumes relative to normal mantle. For example, an isentrope tied to a footing temperature of 2000 K undergoes a temperature increase with depth nearly twice that of an adiabat footed at 1000 K. Consequently, the adiabatic temperature increase in plumes exceeds that of normal mantle by about 300 K [see *Piazzoni et al.*, 2007, Fig. 7]. Combining these two effects suggests that the near surface excess temperature of mantle plumes of around +300 K translates into hot thermal variations on the order of +1000 K in the lowermost mantle, entirely consistent with a strong thermal gradient across the CMB.

The dominance of thermal variations on seismic heterogeneity contrasts with recent interpretations of seismic tomography [*Su and Dziewonski*, 1997; *Masters et al.*, 2000;

Ishii and Tromp, 1999; *Trampert et al.*, 2004]. For example, *Trampert et al.* [2004] have inverted normal mode splitting observations and surface wave data for variations in temperature, perovskite and iron content. Using a probabilistic approach, they find a large likelihood that density variations in the lowermost mantle are dominated by chemical rather than thermal anomalies. However, their inferred temperature variations of ±300 K, and in particular the low excess temperature of hot upwellings in the lowermost mantle, are difficult to understand in light of the above considerations. Our MCMs with strong core heat flux (M2–M4) instead suggest that one can account for the observed amplitudes of seismic heterogeneity in the lowermost mantle by thermal variations and their effects on elasticity. The high plume excess temperatures in the deeper mantle agree with tomographic studies showing a depthwise increase in heterogeneity strength of low seismic velocity anomalies [*Boschi and Dziewonski*, 1999; *Romanowicz and Gung*, 2002; *Montelli et al.*, 2004], and are probably related to independent evidence for ultra-low seismic velocities at the CMB [*Garnero*, 2000], as these temperatures approach the lower mantle solidus. A thermal interpretation of lower mantle seismic velocity anomalies is also favored by recent joint inversions of seismic data, free-air gravity, dynamic topography and excess ellipticity of the CMB [*Simmons et al.*, 2007].

Experimental [*Andrault et al.*, 2001; *Mao et al.*, 1991; *Zhang and Weidner*, 1999] and first-principle results [*Kiefer et al.*, 2002] demonstrate that compositional variations strongly affect the volume and shear modulus of perovskite. Similarly, one observes in (Mg,Fe)O magnesio-wüstite that an increase in iron content significantly lowers the shear modulus [*Lin et al.*, 2006, and references therein]. These findings bear on our models, since Figures 6 and 9 show that the strong positive thermal anomalies, which we infer from the MCMs, imply shear wave anomalies that match and in some cases (M2) exceed the bounds of lower mantle heterogeneity mapped by seismic tomography. A further increase in heterogeneity by further reducing the shear wave velocities would follow, if one assumed iron enrichment in the low velocity regions [*Wang and Weidner*, 1996; *Jackson*, 1998], unless one attributes much lower excess temperatures to them [*Trampert et al.*, 2004].

We note, however, that tomographic studies in general suffer from limited resolving power, only providing a filtered view into Earth's mantle. Imaged velocity anomalies and inferred temperature variations may thus be underestimated. Further comparisons are therefore needed to explore the effects of "tomographic filtering", which are likely to reduce the amplitudes of geodynamically predicted heterogeneity [*Mégnin et al.*, 1997; *Davies and Bunge*, 2001; *Bunge and Davies*, 2001].

5.2. Strong Core Heat Flux

Beyond the considerations on seismic heterogeneity, our results also bear on CMB heat flux. The strongly bottom heated MCMs (M2–M4) predict a substantial core heat loss in the range of 9–12 TW, considerably higher than the heat transport commonly inferred from hotspots [*Davies*, 1988; *Sleep*, 1990]. A number of geodynamic studies have recently supported a significant core heat loss to overcome problems of insufficient internal mantle heat sources [*Kellogg et al.*, 1999], and to satisfy the power requirements of the geodynamo [*Glatzmaier and Roberts*, 1995; *Kuang and Bloxham*, 1997] and estimates of the thermal history of the core [*Buffett*, 2002; *Nimmo et al.*, 2004]. In particular, *Gubbins et al.* [2004] infer a large passive heat transport along the outer-core adiabat of 9 TW from compressible two-component core convection. Additional heat is released from ohmic dissipation in the generation of the magnetic field, for which our current limited understanding provides estimates ranging from 0.1 to 3.5 TW [*Roberts and Glatzmaier*, 2000; *Buffett*, 2002; *Roberts et al.*, 2003; *Labrosse*, 2003; *Gubbins et al.*, 2003; *Christensen and Tilgner*, 2004], The total core heat loss may thus approach 9–12 TW. Specifically, this implies a core contribution to the overall mantle heat budget in the range of 30–40%, and a Urey number of 0.6, much closer to estimates from geochemistry of 0.3–0.5 [*McDonough*, 2007] than classic geodynamical values of ∼0.9–0.95 [*Turcotte and Schubert*, 2001]. Moreover, a substantial core heat loss is also favored by *Nolet et al.* [2006] and would at least in part address the difficulty raised by missing heat production in the mantle [*Urey*, 1956; *Jochum et al.*, 1983].

5.3. Plume Morphology and Lacking Information on the Initial Condition

An important argument in support of chemical heterogeneity is the morphology, or shape, of deep mantle upwellings, taken either from direct observations of seismic data [*Ni et al.*, 2002], or from laboratory [*Jellinek and Manga*, 2004] and numerical studies [*McNamara and Zhong*, 2004]. Unfortunately, the shape of lower mantle structure is poorly constrained by mantle circulation models relying on the sequential assimilation of past plate motions [*Bunge et al.*, 2002; *McNamara and Zhong*, 2005]. The difficulty arises from lack of information on the initial condition [*Bunge et al.*, 2003] and uncertainties in models of plate motion history, which grow larger as one goes back in time. As an example of the latter, we compare Figures 3 and 1. The hot upwelling structure under southern Africa is predicted too far south by our MCM approach (see also the cold downwelling structure under Northeast Africa in Figs. 2 and 3), probably as a result of uncertainties in the convergence history of the African and Eurasian plates. This interpretation is supported by the recent reconstructions of *Müller et al.* [2008], which place the convergent margin farther north than the plate motion history used in our study [*Lithgow-Bertelloni and Richards*, 1998]. Efforts are currently underway to extend models of past plate motions further back in time [*Torsvik et al.*, 2008], and to explore adjoint techniques in geodynamic simulations to better constrain the temporal evolution of the mantle [*Bunge et al.*, 2003; *Ismail-Zadeh et al.*, 2004, 2007; *Liu and Gurnis*, 2008].

6. Conclusions

We have presented global models of thermal and elastic mantle heterogeneity derived from high-resolution mantle circulation modeling involving 80 million finite elements. Variations in seismic velocities are obtained by converting absolute temperatures into elastic heterogeneity using recently published thermodynamically self-consistent models of mantle petrology and elasticity. We find significant differences in the characteristics of thermal and seismic heterogeneity, which warrant a careful geodynamic interpretation of tomographic models. Most importantly, our models make a number of quantitative predictions for statistical properties such as spectral power, histograms and RMS amplitudes, all of which are found in good agreement with tomography. A key observation is the magnitude of lower mantle thermal anomalies (on the order of 1000 K). The corresponding strong reduction in shear wave velocity, which we infer for hot upwelling regions in our models, agrees well with the magnitude of shear wave anomalies mapped by tomography in low velocity regions of the deeper mantle.

Our results suggest that simple isochemical mantle circulation models are capable of explaining some first-order observations from tomography when combined with strong heat flux from the core on the order of 9–12 TW. This number is supported by many recent studies on core and mantle

dynamics, related material properties, as well as by seismological observations. Uncertainties in plate tectonic reconstructions and the unknown initial condition of mantle general circulation, however, limit our capabilities of constraining the geographic pattern of heterogeneity in the lowermost mantle.

The models presented here may be improved in various ways. For example, updated models of plate motion history will help to better constrain the location and morphology of deeper mantle structure. Also, we have not included the effects of horizontal viscosity variations, which are particularly important in the lithosphere in generating shear localisation and plate like behavior through temperature dependent viscosities and plastic yielding [*Trompert and Hansen*, 1998; *Richards et al.*, 2001], although a combination of neotectonic and mantle convection modeling appears effective in modeling the complexities of plate motion [*Iaffaldano et al.*, 2006; *Iaffaldano and Bunge*, 2008].

Furthermore, the mineralogical models currently do not account for the potential presence of post-perovskite, thus limiting conclusions on structure in D". Moreover, we have also excluded any additional complexity arising from chemical variations, choosing to study simple isochemical models first and to isolate thermal effects. Work by *Hutko et al.* [2008] and *Hernlund and Houser* [2008] suggests that at least part of the observed anti-correlation of v_s and v_ϕ, which is difficult to explain from a uniform composition, could be related to the occurrence of post-perovskite. With respect to sharp gradients in seismic structures observed in the lower mantle, and the possibility to explain these by a purely thermal origin, our high-resolution MCMs with their strong lateral variations will have to be filtered to the resolution of tomography for further comparisons.

Finally, tomographic models as well have to be refined, especially in terms of resolving the amplitudes and gradients of heterogeneity. In this respect, various improvements in tomographic imaging techniques are currently investigated, such as finite frequency tomography including waveform amplitude information [*Sigloch et al.*, 2008] or full waveform inversion using adjoint techniques [*Tromp et al.*, 2005; *Fichtner et al.*, 2006a, b].

Acknowledgments. The authors thank Lars Stixrude, Carolina Lithgow-Bertelloni and Antonio Piazzoni for providing their mineralogical models. Furthermore, we thank Ch. Houser, M. Ishii, H. Karason, G. Masters, R. Montelli, J. Ritsema, N. Simmons and W.-J. Su for providing their tomographic models, the NERIES project for offering them in a standardized format on the internet, and two anonymous reviewers for detailed and constructive comments. Figures 1 and 3 were generated with GMT4.0 [*Wessel and Smith*, 1991]. The simulations used in this study were partly computed on the supercomputing facilities of the Leibniz-Rechenzentrum (LRZ) Munich, Germany. We thank the staff of the LRZ for their support. This research was funded by the International Graduate School THESIS within the Elite-Network of Bavaria (BSAS) and the German Science Foundation (DFG) under grants BU 2010/3-1 (HPB) and STE 1105/5-1 (GSN).

References

Alfè, D., G. D. Price, and M. J. Gillan (2002), Iron under earth's core conditions: Liquid-state thermodynamics and high-pressure melting curve from ab initio calculations, *Physical Review B*, *65*(16), 165,118–165,129, doi:10.1103/PhysRevB.65.165118.

Alfè, D., M. J. Gillan, and G. D. Price (2007), Temperature and composition of the earth's core, *Contemporary Physics*, *48*(2), 63–80, doi:10.1080/00107510701529653.

Andrault, D., N. Bolfan-Casanova, and N. Guignot (2001), Equation of state of lower mantle (Al,Fe)-MgSiO3 perovskite, *Earth Planet. Sci. Lett.*, *193*(3-4), 501–508, doi:10.1016/S0012-821X(01)00506-4.

Becker, T. W., and R. J. O'Connell (2001), Predicting plate velocities with mantle circulation models, *Geochem. Geophys. Geosyst.*, *2*(12), doi:10.1029/2001GC000171, 2001.

Boehler, R. (2000), High-pressure experiments and the phase diagram of lower mantle and core materials, *Rev. Geophys.*, *38*(2), 221–245.

Boschi, L., and A. M. Dziewonski (1999), High- and low-resolution images of the earth's mantle: Implications of different approaches to tomographic modeling, *J. Geophys. Res.*, *104*(B11), 25,567–25,594.

Buffett, B. A. (2002), Estimates of heat flow in the deep mantle based on the power requirements for the geodynamo, *Geophys. Res. Lett.*, *29*(12), 1566, doi:10.1029/2001GL014649.

Bunge, H. P. (1996), Global mantle convection models, Ph.D. thesis, University of California, Berkeley.

Bunge, H. P. (2005), Low plume excess temperature and high core heat flux inferred from non-adiabatic geotherms in internally heated mantle circulation models, *Phys. Earth Planet. Inter.*, *153*(1-3), 3–10, doi:10.1016/j.pepi.2005.03.017.

Bunge, H.-P., and J. Baumgardner (1995), Mantle convection modeling on parallel virtual machines, *Computers in Physics*, *9*, 207–215.

Bunge, H. P., and J. H. Davies (2001), Tomographic images of a mantle circulation model, *Geophys. Res. Lett.*, *28*(1), 77–80.

Bunge, H.-P., and M. Richards (1996), The origin of large-scale structure in mantle convection: effects of plate motions and viscosity stratification, *Geophys. Res. Lett.*, *23*, 2987–2990.

Bunge, H.-P., M. Richards, and J. Baumgardner (1996), The effect of depth-dependent viscosity on the planform of mantle convection, *Nature*, *379*, 436–438, doi:10.1038/379436a0.

Bunge, H.-P., M. Richards, and J. Baumgardner (1997), A sensitivity study of 3D-spherical mantle convection at 10exp8 rayleigh number: effects of depth-dependent viscosity, heating mode and an endothermic phase change, *J. Geophys. Res.*, *102*, 11,991–12,007.

Bunge, H.-P., M. Richards, C. Lithgow-Bertelloni, J. Baumgardner, S. Grand, and B. Romanowicz (1998), Time scales and heterogeneous structure in geodynamic earth models, *Science*, *280*, 91–95, doi:10.1126/science.280.5360.91.

Bunge, H. P., Y. Ricard, and J. Matas (2001), Non-adiabaticity in mantle convection, *Geophys. Res. Lett.*, *28*(5), 879–882.

Bunge, H.-P., M. Richards, and J. Baumgardner (2002), Mantle circulation models with sequential data-assimilation: Inferring present-day mantle structure from plate motion histories, *Phil. Trans. Roy. Soc. A*, *360*(1800), 2545–2567, doi:10.1098/rsta.2002.1080.

Bunge, H.-P., C. R. Hagelberg, and B. J. Travis (2003), Mantle circulation models with variational data-assimilation: Inferring past mantle flow and structure from plate motion histories and seismic tomography, *Geophys. J. Int.*, *2*(152), 280–301, doi:10.1046/j.1365-246X.2003.01823.x.

Cammarano, F., S. Goes, P. Vacher, and D. Giardini (2003), Inferring upper-mantle temperatures from seismic velocities, *Phys. Earth Planet. Inter.*, *138*(3-4), 197–222, doi:10.1016/S0031-9201(03)00156-0.

Christensen, U. R., and A. W. Hofmann (1994), Segregation of subducted oceanic-crust in the convecting mantle, *J. Geophys. Res.*, *99*(B10), 19,867–19,884.

Christensen, U. R., and A. Tilgner (2004), Power requirement of the geodynamo from ohmic losses in numerical and laboratory dynamos, *Nature*, *429*(6988), 169–171, doi:10.1038/nature02508.

Conrad, C. P., and C. Lithgow-Bertelloni (2002), How mantle slabs drive plate tectonics, *Science*, *298*(5591), 207–209, doi:10.1126/science.1074161.

Dahlen, F. A., and J. Tromp (1998), *Theoretical Global Seismology*, Princeton University Press, Princeton, New Jersey.

Davaille, A. (1999), Simultaneous generation of hotspots and superswells by convection in a heterogenous planetary mantle, *Nature*, *402*(6763), 756–760, doi:10.1038/45461.

Davaille, A., F. Girard, and M. Le Bars (2002), How to anchor hotspots in a convecting mantle?, *Earth Planet. Sci. Lett.*, *203*(2), 621–634, doi:10.1016/S0012-821X(02)00897-X.

Davies, G. F. (1988), Ocean bathymetry and mantle convection 1. Large-scale flow and hotspots, *J. Geophys. Res.*, *93*(B9), 10,467–10,480.

Davies, J. H., and H. P. Bunge (2001), Seismically "fast" geodynamic mantle models, *Geophys. Res. Lett.*, *28*(1), 73–76.

Deschamps, F., and J. Trampert (2003), Mantle tomography and its relation to temperature and composition, *Phys. Earth Planet. Inter.*, *140*(4), 277–291, doi:10.1016/j.pepi.2003.09.004.

Deschamps, F., and J. Trampert (2004), Towards a lower mantle reference temperature and composition, *Earth Planet. Sci. Lett.*, *222*(1), 161–175, doi:10.1016/j.epsl.2004.02.024.

Dziewonski, A. M., and D. L. Anderson (1981), Preliminary reference Earth model, *Phys. Earth Planet. Inter.*, *25*, 297–356, doi:10.1016/0031-9201(81)90046-7.

Farnetani, C. G., and H. Samuel (2005), Beyond the thermal plume paradigm, *Geophys. Res. Lett.*, *32*(7), L07,311, doi:10.1029/2005GL022360.

Fichtner, A., H.-P. Bunge, and H. Igel (2006a), The adjoint method in seismology: I - Theory, *Phys. Earth Planet. Inter.*, *157*(1-2), 86–104, doi:10.1016/j.pepi.2006.03.016.

Fichtner, A., P. Bunge, and H. Igel (2006b), The adjoint method in seismology: II - Applications: traveltimes and sensitivity functionals, *Phys. Earth Planet. Inter.*, *157*(1-2), 105–123, doi:10.1016/j.pepi.2006.03.018.

Garnero, E. J. (2000), Heterogeneity of the lowermost mantle, *Annual Review of Earth and Planetary Sciences*, *33*, 1–66, doi:10.1146/annurev.earth.28.1.509.

Glatzmaier, G. A. (1988), Numerical simulations of mantle convection - time-dependent, 3-dimensional, compressible, spherical-shell, *Geophysical And Astrophysical Fluid Dynamics*, *43*(2), 223–264, doi:10.1080/03091928808213626.

Glatzmaier, G. A., and P. H. Roberts (1995), A 3-dimensional self-consistent computer-simulation of a geomagnetic-field reversal, *Nature*, *377*(6546), 203–209, doi:10.1038/377203a0.

Goes, S., F. Cammarano, and U. Hansen (2004), Synthetic seismic signature of thermal mantle plumes, *Earth Planet. Sci. Lett.*, *218*(3-4), 403–419, doi:10.1016/S0012-821X(03)00680-0.

Grand, S., R. van der Hilst, and S. Widiyantoro (1997), Global seismic tomography: A snapshot of mantle convection in the earth, *GSA Today*, *7*, 1–7.

Gubbins, D., D. Alfe, G. Masters, G. D. Price, and M. J. Gillan (2003), Can the Earth's dynamo run on heat alone?, *Geophys. J. Int.*, *155*(2), 609–622, doi:10.1046/j.1365-246X.2003.02064.x.

Gubbins, D., D. Alfe, G. Masters, G. D. Price, and M. Gillan (2004), Gross thermodynamics of two-component core convection, *Geophys. J. Int.*, *157*(3), 1407–1414, doi:10.1111/j.1365-246X.2004.02219.x.

Hager, B. H., and M. A. Richards (1989), Long-wavelength variations in earths geoid - physical models and dynamical implications, *Phil. Trans. Roy. Soc. A*, *328*(1599), 309–327, doi:10.1098/rsta.1989.0038.

Hansen, U., and D. A. Yuen (1989), Dynamical influences from thermal-chemical instabilities at the core-mantle boundary, *Geophys. Res. Lett.*, *16*(7), 629–632.

Hansen, U., and D. A. Yuen (1994), Effects of depth-dependent thermal expansivity on the interaction of thermal-chemical plumes with a compositional boundary, *Phys. Earth Planet. Inter.*, *86*(1-3), 205–221, doi:10.1016/0031-9201(94)05069-4.

Hansen, U., and D. A. Yuen (2000), Extended-Boussinesq thermal-chemical convection with moving heat sources and variable viscosity, *Earth Planet. Sci. Lett.*, *176*(3-4), 401–411, doi:10.1016/S0012-821X(00)00009-1.

Hernlund, J. W., and C. Houser (2008), On the statistical distribution of seismic velocities in earth's deep mantle, *Earth Planet. Sci. Lett.*, *265*(3-4), 423–437, doi:10.1016/j.epsl.2007.10.042.

Houser, C., G. Masters, P. Shearer, and G. Laske (2008), Shear and compressional velocity models of the mantle from cluster analysis of long-period waveforms, *Geophys. J. Int.*, *174*(1), 195–212, doi:10.1111/j.1365-246X.2008.03763.x.

Hutko, A. R., T. Lay, J. Revenaugh, and E. J. Garnero (2008), Anticorrelated seismic velocity anomalies from post-perovskite in the lowermost mantle, *Science*, *320*(5879), 1070–1074, doi:10.1126/science.1155822.

Iaffaldano, G., and H.-P. Bunge (2008), Strong plate coupling along the Nazca-South America convergent margin, *Geology*, *36*(6), 443–446, doi:10.1130/G24489A.1.

Iaffaldano, G., H.-P. Bunge, and T. H. Dixon (2006), Feedback between mountain belt growth and plate convergence, *Geology*, *34*(10), 893–896, doi:10.1130/G22661.1.

Irifune, T. (1987), An experimental investigation of the pyroxene garnet transformation in a pyrolite composition and its bearing on the constitution of the mantle, *Phys. Earth Planet. Inter.*, *45*(4), 324–336, doi:10.1016/0031-9201(87)90040-9.

Ishii, M., and J. Tromp (1999), Normal-Mode and Free-Air Gravity Constraints on Lateral Variations in Velocity and Density of Earth's Mantle, *Science*, *285*(5431), 1231–1236, doi:10.1126/science.285.5431.1231.

Ishii, M., and J. Tromp (2001), Even-degree lateral variations in the earth's mantle constrained by free oscillations and the free-air gravity anomaly, *Geophys. J. Int.*, *145*(1), 77–96, doi:10.1111/j.1365-246X.2001.00385.x.

Ismail-Zadeh, A., G. Schubert, I. Tsepelev, and A. Korotkii (2004), Inverse problem of thermal convection: numerical approach and application to mantle plume restoration, *Phys. Earth Planet. Inter.*, *145*(1-4), 99–114, doi:10.1016/j.pepi.2004.03.006.

Ismail-Zadeh, A., A. Korotkii, G. Schubert, and I. Tsepelev (2007), Quasi-reversibility method for data assimilation in models of mantle dynamics, *Geophys. J. Int.*, *170*(3), 1381–1398, doi:10.1111/j.1365-246X.2007.03496.x.

Jackson, I. (1998), Elasticity, composition and temperature of the earth's lower mantle: a reappraisal, *Geophys. J. Int.*, *134*(1), 291–311, doi:10.1046/j.1365-246x.1998.00560.x.

Jarvis, G. T., and D. P. McKenzie (1980), Convection in a compressible fluid with infinite Prandtl number, *Journal Of Fluid Mechanics*, *96*(FEB), 515–583, doi:10.1017/S002211208000225X.

Jeanloz, R., and S. Morris (1987), Is the mantle geotherm subadiabatic, *Geophys. Res. Lett.*, *14*(4), 335–338.

Jellinek, A. M., and M. Manga (2004), Links between long-lived hot spots, mantle plumes, D", and plate tectonics, *Rev. Geophys.*, *42*, RG3002, doi:10.1029/2003RG000144.

Jochum, K. P., A. W. Hofmann, E. Ito, H. M. Seufert, and W. M. White (1983), K, U and Th in mid-ocean ridge basalt glasses and heat-production, K/U and K/Rb in the mantle, *Nature*, *306*(5942), 431–436, doi:10.1038/306431a0.

Jordan, T. H., P. Puster, G. A. Glatzmaier, and P. J. Tackley (1993), Comparisons between seismic earth structures and mantle flow models based on radial correlation-functions, *Science*, *261*(5127), 1427–1431, doi:10.1126/science.261.5127.1427.

Kárason, H., and R. D. van der Hilst (2001), Tomographic imaging of the lowermost mantle with differential times of refracted and diffracted core phases (PKP, Pdiff), *J. Geophys. Res.*, *106*, 6569–6588.

Kellogg, L. H., B. H. Hager, and R. D. van der Hilst (1999), Compositional stratification in the deep mantle, *Science*, *283*(5409), 1881–1884, doi:10.1126/science.283.5409.1881.

Kennett, B. L. N., E. R. Engdahl, and R. Buland (1995), Constraints on seismic velocities in the earth from traveltimes, *Geophys. J. Int.*, *122*(1), 108–124, doi:10.1111/j.1365-246X.1995.tb03540.x.

Kennett, B. L. N., S. Widiyantoro, and R. D. van der Hilst (1998), Joint seismic tomography for bulk sound and shear wave speed in the earth's mantle, *J. Geophys. Res.*, *103*(B6), 12,469–12,493.

Kiefer, B., L. Stixrude, and R. M. Wentzcovitch (2002), Elasticity of (Mg,Fe)SiO3-perovskite at high pressures, *Geophys. Res. Lett.*, *29*(11), 1539, doi:doi:10.1029/2002GL014683.

Kuang, W. L., and J. Bloxham (1997), An earth-like numerical dynamo model, *Nature*, *389*(6649), 371–374, doi:10.1038/38712.

Labrosse, S. (2003), Thermal and magnetic evolution of the earth's core, *Phys. Earth Planet. Inter.*, *140*(1-3), 127–143, doi:10.1016/j.pepi.2003.07.006.

Lay, T. (2008), Sharpness of the D" discontinuity beneath the Cocos Plate: Implications for the perovskite to post-perovskite phase transition, *Geophys. Res. Lett.*, *35*, L03,304, doi:10.1029/2007GL032465.

Li, X. D., and B. Romanowicz (1996), Global mantle shear velocity model developed using nonlinear asymptotic coupling theory, *J. Geophys. Res.*, *101*(B10), 22,245–22,272.

Lin, J. F., S. D. Jacobsen, W. Sturhahn, J. M. Jackson, J. Y. Zhao, and C. S. Yoo (2006), Sound velocities of ferropericlase in the Earth's lower mantle, *Geophys. Res. Lett.*, *33*(22), L22,304, doi:10.1029/2006GL028099.

Lithgow-Bertelloni, C., and M. A. Richards (1998), The dynamics of Cenozoic and Mesozoic plate motions, *Rev. Geophys.*, *36*(1), 27–78.

Liu, L. J., and M. Gurnis (2008), Simultaneous inversion of mantle properties and initial conditions using an adjoint of mantle convection, *J. Geophys. Res.*, *113*(B8), B08,405, doi:10.1029/2008JB005594.

Mao, H. K., R. J. Hemley, Y. Fei, J. F. Shu, L. C. Chen, A. P. Jephcoat, Y. Wu, and W. A. Bassett (1991), Effect of pressure, temperature, and composition on lattice-parameters and density of (Fe,Mg)SiO3-perovskites to 30 gpa, *J. Geophys. Res.*, *96*(B5), 8069–8079.

Masters, G., S. Johnson, G. Laske, H. Bolton, and J. H. Davies (1996), A shear-velocity model of the mantle, *Phil. Trans. Roy. Soc. A*, *354*(1711), 1385–1410, doi:10.1098/rsta.1996.0054.

Masters, G., G. Laske, H. Bolton, and A. M. Dziewonski (2000), *Eearth's Deep Interior – Mineral Physics and Tomography From the Atomic to the Global Scale*, chap. The Relative Behavior of Shear Velocity, Bulk Sound Speed, and Compressional Velocity in the Mantle: Implications for Chemical and Thermal Structure, pp. 63–87, American Geophysical Union, Washington D.C.

Matas, J., J. Bass, Y. Ricard, E. Mattern, and M. S. T. Bukowinski (2007), On the bulk composition of the lower mantle: predictions and limitations from generalized inversion of radial seismic profiles, *Geophys. J. Int.*, *170*, 764–780, doi:10.1111/j.1365-246X.2007.03454.x.

Mattern, E., J. Matas, Y. Ricard, and J. Bass (2005), Lower mantle composition and temperature from mineral physics and thermodynamic modelling, *Geophys. J. Int.*, *160*(3), 973–990, doi:10.1111/j.1365-246X.2004.02549.x.

Matyska, C., and D. A. Yuen (2000), Profiles of the Bullen parameter from mantle convection modelling, *Earth Planet. Sci. Lett.*, *178*(1-2), 39–46, doi:10.1016/S0012-821X(00)00060-1.

McDonough, W. F. (2007), Mapping the earth's engine, *Science*, *317*(5842), 1177–1178, doi:10.1126/science.1144405.

McKenzie, D., and M. J. Bickle (1988), The volume and composition of melt generated by extension of the lithosphere, *J. Petrology*, *29*(3), 625–679.

McNamara, A., and S. Zhong (2005), Thermochemical structures beneath Africa and the Pacific Ocean, *Nature*, *437*, 1136–1139, doi:10.1038/nature04066.

McNamara, A. K., and S. J. Zhong (2004), Thermochemical structures within a spherical mantle: Superplumes or piles?, *J. Geophys. Res.*, *109*(B7), B07,402, doi:10.1029/2003JB002847.

McNamara, A. K., P. E. van Keken, and S. I. Karato (2002), Development of anisotropic structure in the earth's lower mantle by solid-state convection, *Nature*, *416*(6878), 310–314, doi:10.1038/416310a.

Mégnin, C., H.-P. Bunge, B. Romanowicz, and M. Richards (1997), Imaging 3-D spherical convection models: what can seismic tomography tell us about mantle dynamics?, *Geophys. Res. Lett.*, *24*(11), 1299–1302, doi:10.1029/97GL01256.

Mitrovica, J. X. (1996), Haskell [1935] revisited, *J. Geophys. Res.*, *101*(B1), 555–569.

Mittelstaedt, E., and P. J. Tackley (2006), Plume heat flow is much lower than cmb heat flow, *Earth Planet. Sci. Lett.*, *241*(1-2), 202–210, doi:10.1016/j.epsl.2005.10.012.

Monnereau, M., and D. A. Yuen (2002), How flat is the lower-mantle temperature gradient?, *Earth Planet. Sci. Lett.*, *202*(1), 171–183, doi:10.1016/S0012-821X(02)00756-2.

Montague, N. L., and L. H. Kellogg (2000), Numerical models of a dense layer at the base of the mantle and implications for the geodynamics of D", *J. Geophys. Res.*, *105*(B5), 11,101–11,114.

Montelli, R., G. Nolet, F. A. Dahlen, G. Masters, E. R. Engdahl, and S.-H. Hung (2004), Finite-Frequency Tomography Reveals a Variety of Plumes in the Mantle, *Science*, *303*(5656), 338–343, doi:10.1126/science.1092485.

Montelli, R., G. Nolet, F. A. Dahlen, and G. Masters (2006), A catalogue of deep mantle plumes: New results from finite-frequency tomography, *Geochem. Geophys. Geosyst.*, *7*, Q11,007, doi:10.1029/2006GC001248.

Müller, R., M. Sdrolias, C. Gaina, and W. Roest (2008), Age, spreading rates and spreading asymmetry of the world's ocean crust, *Geochem. Geophys. Geosyst.*, *9*(4), doi:10.1029/2007GC001743.

Murnaghan, F. (1951), *Finite Deformation of an Elastic Solid*, Wiley, New York.

Nakagawa, T., and P. J. Tackley (2004), Thermo-chemical structure in the mantle arising from a three-component convective system and implications for geochemistry, *Phys. Earth Planet. Inter.*, *146*(1-2), 125–138, doi:10.1016/j.pepi.2003.05.006.

Ni, S., and D. V. Helmberger (2003), Further constraints on the african superplume structure, *Phys. Earth Planet. Inter.*, *140*(1-3), 243–251, doi:10.1016/j.pepi.2003.07.011.

Ni, S. D., E. Tan, M. Gurnis, and D. V. Helmberger (2002), Sharp sides to the African superplume, *Science*, *296*, 1850–1852, doi:10.1126/science.1070698.

Nimmo, F., G. D. Price, J. Brodholt, and D. Gubbins (2004), The influence of potassium on core and geodynamo evolution, *Geophys. J. Int.*, *156*(2), 363–376, doi:10.1111/j.1365-246X.2003.02157.x.

Nolet, G., S. I. Karato, and R. Montelli (2006), Plume fluxes from seismic tomography, *Earth Planet. Sci. Lett.*, *248*, 685–699, doi:10.1016/j.epsl.2006.06.011.

Oeser, J., H. P. Bunge, and M. Mohr (2006), Cluster design in the earth sciences - Tethys, *High Performance Computing And Communications, Proceedings*, *4208*, 31–40.

Paulson, A., S. J. Zhong, and J. Wahr (2007), Inference of mantle viscosity from GRACE and relative sea level data, *Geophys. J. Int.*, *171*(2), 497–508, doi:10.1111/j.1365-246X.2007.03556.x.

Piazzoni, A. S., G. Steinle-Neumann, H.-P. Bunge, and D. Dolej (2007), A mineralogical model for density and elasticity of the earth's mantle, *Geochem. Geophys. Geosyst.*, *8*, doi:10.1029/2007GC001697.

Presnall, D. C., and G. H. Gudfinnsson (2008), Origin of the oceanic lithosphere, *Journal Of Petrology*, *49*(4), 615–632, doi:10.1093/petrology/egm052.

Resovsky, J., and J. Trampert (2003), Using probabilistic seismic tomography to test mantle velocity-density relationships, *Earth Planet. Sci. Lett.*, *215*(1-2), 121–134, doi:10.1016/S0012-821X(03)00436-9.

Ricard, Y., E. Mattern, and J. Matas (2005), *Earth's Deep Mantle: Structure, Composition, and Evolution*, chap. Synthetic Tomographic Images of Slabs From Mineral Physics, pp. 285–302, American Geophysical Union.

Richards, M. A., and D. C. Engebretson (1992), Large-scale mantle convection and the history of subduction, *Nature*, *355*(6359), 437–440, doi:10.1038/355437a0.

Richards, M. A., W. S. Yang, J. R. Baumgardner, and H. P. Bunge (2001), Role of a low-viscosity zone in stabilizing plate tectonics: Implications for comparative terrestrial planetology, *Geochem. Geophys. Geosyst.*, *2*, GC000,115.

Ringwood, A. E. (1975), *Composition and Petrology of the Earth's Mantle*, McGraw-Hill Company, New York, bb55.

Ritsema, J., and H. J. Van Heijst (2000), Seismic imaging of structural heterogeneity in Earth's mantle: Evidence for large-scale mantle flow, *Science Progress*, *83*, 243–259.

Ritsema, J., and H. J. van Heijst (2002), Constraints on the correlation of P- and S-wave velocity heterogeneity in the mantle from P, PP, PPP and PKPab traveltimes, *Geophys. J. Int.*, *149*(2), 482–489, doi:10.1046/j.1365-246X.2002.01631.x.

Ritsema, J., H. J. Van Heijst, and J. H. Woodhouse (1999), Complex shear velocity structure imaged beneath Africa and Iceland, *Science*, *286*, 1925–1928, doi:10.1126/science.286.5446.1925.

Ritsema, J., H. J. van Heijst, and J. H. Woodhouse (2004), Global transition zone tomography, *J. Geophys. Res.*, *109*(B2), doi:10.1029/2003JB002610.

Roberts, P. H., and G. A. Glatzmaier (2000), A test of the frozen-flux approximation using a new geodynamo model, *Phil. Trans. R. Soc. Lond.*, *358*(1768), 1109–1121, doi:10.1098/rsta.2000.0576.

Roberts, P. H., C. A. Jones, and A. R. Calderwood (2003), Energy fluxes and ohmic dissipation in the earth's core, *Earth's Core And Lower Mantle*, *11*, 100–129.

Romanowicz, B., and Y. C. Gung (2002), Superplumes from the core-mantle boundary to the lithosphere: implications for heat flux, *Science*, *296*, 513–516, doi:10.1126/science.1069404.

Schilling, J. G. (1991), Fluxes and excess temperatures of mantle plumes inferred from their interaction with migrating midocean ridges, *Nature*, *352*(6334), 397–403, doi:10.1038/352397a0.

Sigloch, K., N. McQuarrie, and G. Nolet (2008), Two-stage subduction history under North America inferred from multiple-frequency tomography, *Nature Geoscience*, doi:10.1038/ngeo231.

Simmons, N. A., A. M. Forte, and S. P. Grand (2007), Thermochemical structure and dynamics of the African superplume, *Geophys. Res. Lett.*, *34*, L02,301, doi:doi:10.1029/2006GL028009.

Sleep, N. H. (1990), Hotspots and mantle plumes - some phenomenology, *J. Geophys. Res.*, *95*(B5), 6715–6736.

Sleep, N. H. (2003), Simple features of mantle-wide convection and the interpretation of lower-mantle tomograms, *Comptes Rendus Geoscience*, *335*(1), 9–22, doi:10.1016/S1631-0713(03)00008-7.

Staudigel, H., K. H. Park, M. Pringle, J. L. Rubenstone, W. H. F. Smith, and A. Zindler (1991), The longevity of the South-Pacific isotopic and thermal anomaly, *Earth Planet. Sci. Lett.*, *102*(1), 24–44, doi:10.1016/0012-821X(91)90015-A.

Stegman, D. R., M. A. Richards, and J. R. Baumgardner (2002), Effects of depth-dependent viscosity and plate motions on maintaining a relatively uniform mid-ocean ridge basalt reservoir in whole mantle flow, *J. Geophys. Res.*, *107*(B6), 2116, doi:10.1029/2001JB000192.

Steinberger, B. (2000), Slabs in the lower mantle - results of dynamic modelling compared with tomographic images and the geoid, *Phys. Earth Planet. Inter.*, *118*(3-4), 241–257, doi:10.1016/S0031-9201(99)00172-7.

Steinberger, B., and R. Holme (2008), Mantle flow models with core-mantle boundary constraints and chemical heterogeneities in the lowermost mantle, *J. Geophys. Res.*, *113*(B5), B05,403, doi:10.1029/2007JB005080.

Steinle-Neumann, G., L. Stixrude, R. E. Cohen, and O. Gulseren (2001), Elasticity of iron at the temperature of the earth's inner core, *Nature*, *413*(6851), 57–60, doi:10.1038/35092536.

Stixrude, L., and C. Lithgow-Bertelloni (2005), Thermodynamics of mantle minerals - I. Physical properties, *Geophys. J. Int.*, *162*(2), 610–632, doi:10.1111/j.1365-246X.2005.02642.x.

Stixrude, L., and C. Lithgow-Bertelloni (2007), Influence of phase transformations on lateral heterogeneity and dynamics in earth's mantle, *Earth Planet. Sci. Lett.*, *263*, 45–55, doi:10.1016/j.epsl.2007.08.027.

Su, W.-j., and A. M. Dziewonski (1997), Simultaneous inversion for 3-D variations in shear and bulk velocity in the mantle, *Phys. Earth Planet. Inter.*, *100*(1-4), 135–156, doi:10.1016/S0031-9201(96)03236-0.

Tackley, P. J. (2000), Mantle convection and plate tectonics: Toward an integrated physical and chemical theory, *Science*, *288*(5473), 2002–2007, doi:10.1126/science.288.5473.2002.

Tackley, P. J. (2002), Strong heterogeneity caused by deep mantle layering, *Geochem. Geophys. Geosyst.*, *3*, 1024, doi:10.1029/2001GC000167.

Talagrand, O. (1997), Assimilation of observations, an introduction, *Journal Of The Meteorological Society Of Japan*, *75*(1B), 191–209.

Torsvik, T. H., R. D. Müller, R. V. der Voo, B. Steinberger, and C. Gaina (2008), Global plate motion frames: Toward a unified model, *Rev. Geophys.*, *46*, RG3004, doi:10.1029/2007RG000227.

Trampert, J., P. Vacher, and N. Vlaar (2001), Sensitivities of seismic velocities to temperature, pressure and composition in the lower mantle, *Phys. Earth Planet. Inter.*, *124*(3-4), 255–267, doi:10.1016/S0031-9201(01)00201-1.

Trampert, J., F. Deschamps, J. Resovsky, and D. Yuen (2004), Probabilistic tomography maps chemical heterogeneities throughout the lower mantle, *Science*, *306*(5697), 853–856, doi:10.1126/science.1101996.

Tromp, J., C. Tape, and Q. Y. Liu (2005), Seismic tomography, adjoint methods, time reversal and banana-doughnut kernels, *Geophys. J. Int.*, *160*(1), 195–216, doi:10.1111/j.1365-246X.2004.02453.x.

Trompert, R., and U. Hansen (1998), Mantle convection simulations with rheologies that generate plate-like behaviour, *Nature*, *395*(6703), 686–689.

Turcotte, D. L., and G. Schubert (2001), *Geodynamics*, 528 pp., Cambridge University Press, second edition.

Urey, H. C. (1956), The cosmic abundances of potassium, uranium, and thorium and the heat balances of the earth, the moon, and mars, *Proceedings Of The National Academy Of Sciences Of The United States Of America*, *42*(12), 889–891.

van der Hilst, R. D., and H. Karason (1999), Compositional heterogeneity in the bottom 1000 kilometers of earth's mantle: Toward a hybrid convection model, *Science*, *283*(5409), 1885–1888, doi:10.1126/science.283.5409.1885.

van der Hilst, R. D., S. Widiyantoro, and E. R. Engdahl (1997), Evidence for deep mantle circulation from global tomography, *Nature*, *386*(6625), 578–584, doi:10.1038/386578a0.

van der Hilst, R. D., M. V. de Hoop, P. Wang, S. H. Shim, P. Ma, and L. Tenorio (2007), Seismostratigraphy and thermal structure of earth's core-mantle boundary region, *Science*, *315*, 1813–1817, doi:10.1126/science.1137867.

Wang, Y., and L. Wen (2004), Mapping the geometry and geographic distribution of a very low velocity province at the base of the earth's mantle, *J. Geophys. Res.*, *109*(B10), B10,305, doi:10.1029/2003JB002674.

Wang, Y. B., and D. J. Weidner (1996), $(\frac{\partial \mu}{\partial T})_P$ of the lower mantle, *Pure Appl. Geophys.*, *146*(3-4), 533–549, doi:10.1007/BF00874732.

Wen, L. X., P. G. Silver, D. James, and R. Kuehnel (2001), Seismic evidence for a thermo-chemical boundary at the base of the Earth's mantle, *Earth Planet. Sci. Lett.*, *189*, 141–153, doi:10.1016/S0012-821X(01)00365-X.

Wessel, P., and W. H. F. Smith (1991), Free software helps map and display data, *EOS Trans. AGU*, *72*(441), 441.

Yanagisawa, T., and Y. Hamano (1999), "skewness" of s-wave velocity in the mantle, *Geophys. Res. Lett.*, *26*(6), 791–794.

Zhang, J. Z., and D. J. Weidner (1999), Thermal equation of state of aluminum-enriched silicate perovskite, *Science*, *284*(5415), 782–784, doi:10.1126/science.284.5415.782.

Zhong, S. J. (2006), Constraints on thermochemical convection of the mantle from plume heat flux, plume excess temperature, and upper mantle temperature, *J. Geophys. Res.*, *111*(B4), B04,409, doi:10.1029/2005JB003972.

Bernhard Schuberth, Department of Earth and Environmental Sciences, Ludwig-Maximilians-Universität München, Theresienstr. 41, 80333 Munich, Germany. (mail@bernhard-schuberth.de)

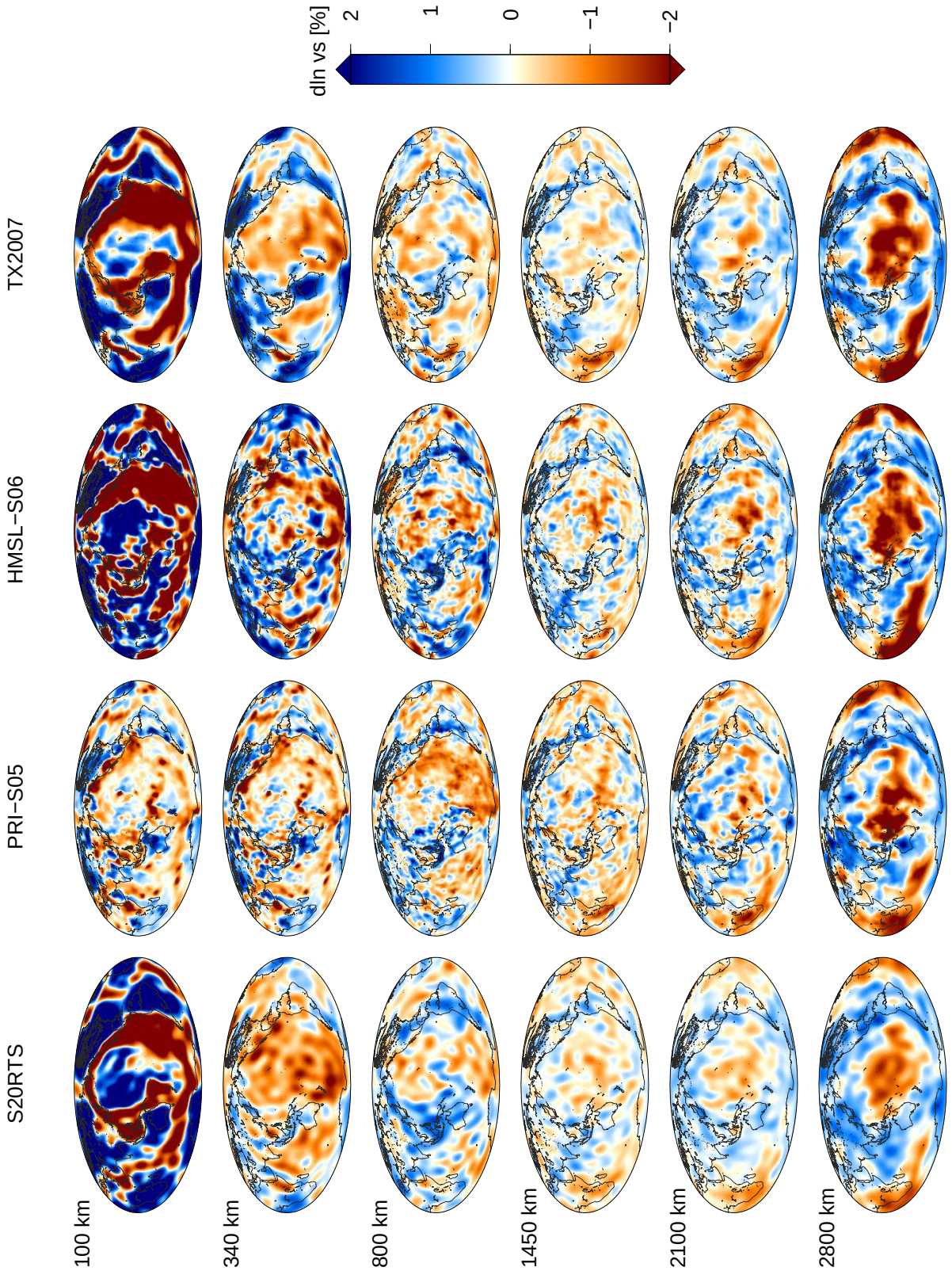

Figure 1. Depth slices through tomographic mantle models of shear wave velocity S20RTS [*Ritsema et al.*, 2004], PRI-S05 [*Montelli et al.*, 2006], HMSL-S06 [*Houser et al.*, 2008], TX2007 [*Simmons et al.*, 2007]. Variations in S-wave velocity are given relative to each corresponding 1-D radial seismic reference model. The color scale ranges from −2% to +2% as shown on the right. Heterogeneity is strongest in the lithosphere, the upper mantle and near the CMB. Note the dynamically important slow seismic velocity structures located under the Pacific and Africa in lowermost mantle (called 'Large Low Velocity Provinces" or "superplumes") and the ring of fast velocities around the Pacific.

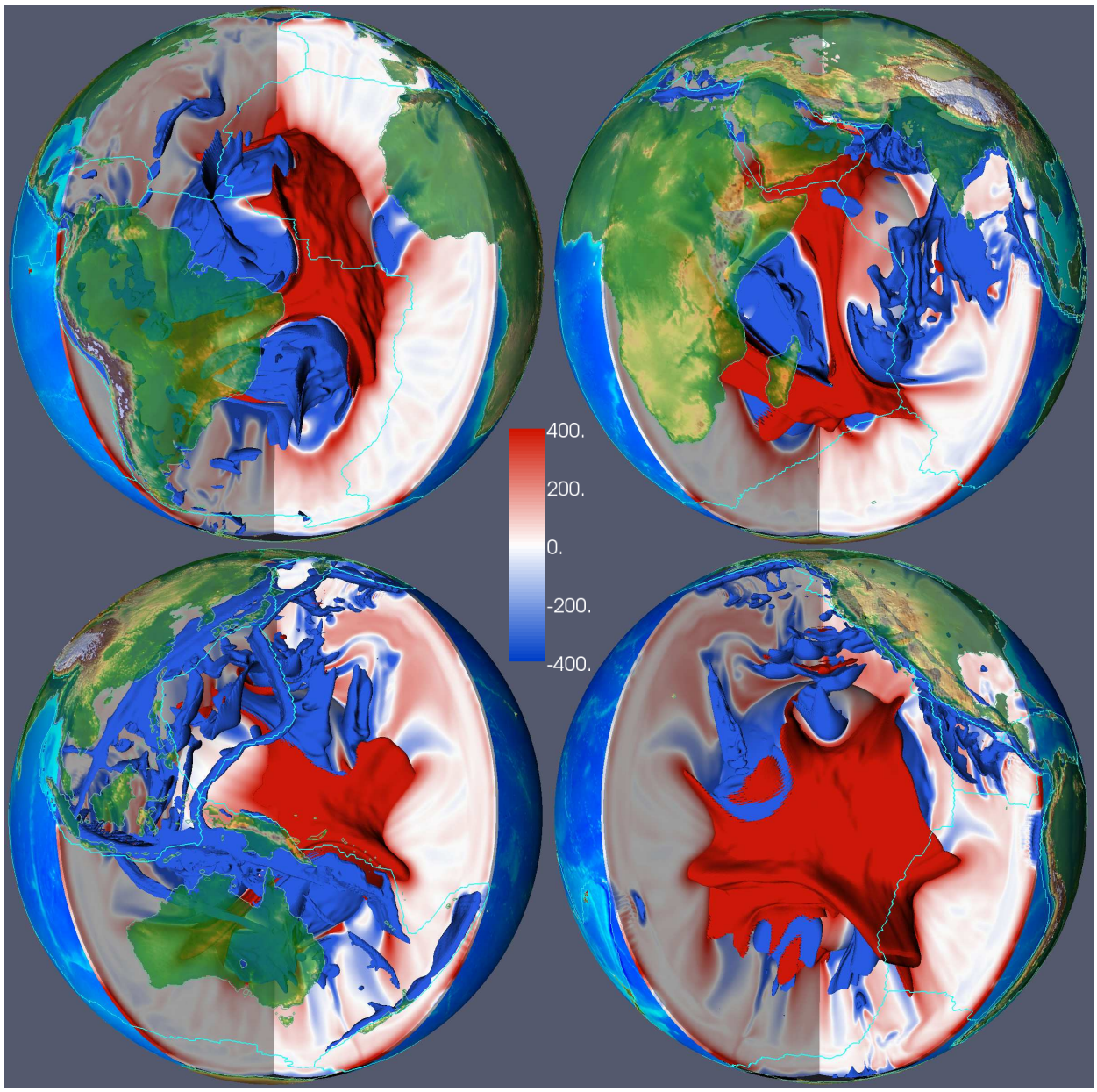

Figure 2. Three-dimensional representation of temperature variations in model M2 with strong core heat flux (see text). The four adjacent cross sections are centered on 35 (upper left), 125 (lower right), 215 (lower left) and 305 (upper right) degrees longitude. The color scale is saturated at −400 K and +400 K, and continents with color-coded topography and plate boundaries (cyan lines) are overlain for geographic reference. Isosurfaces of temperature are displayed for −600 K and +400 K. The +400 K isosurface is clipped in the uppermost 500 km to allow views into the mantle underneath the mid-ocean ridge system, which spans large parts of the oceanic upper mantle. The reduced thermal heterogeneity in the upper mantle (thin, almost white band best visible in the views centered on 125 and 215 degrees longitude) is a consequence of the lower viscosity, there. Note also the prominent thermal upwelling in the Eastern and Central Pacific not far from the SOPITA anomaly identified on thermal and geochemical grounds by *Staudigel et al.* [1991].

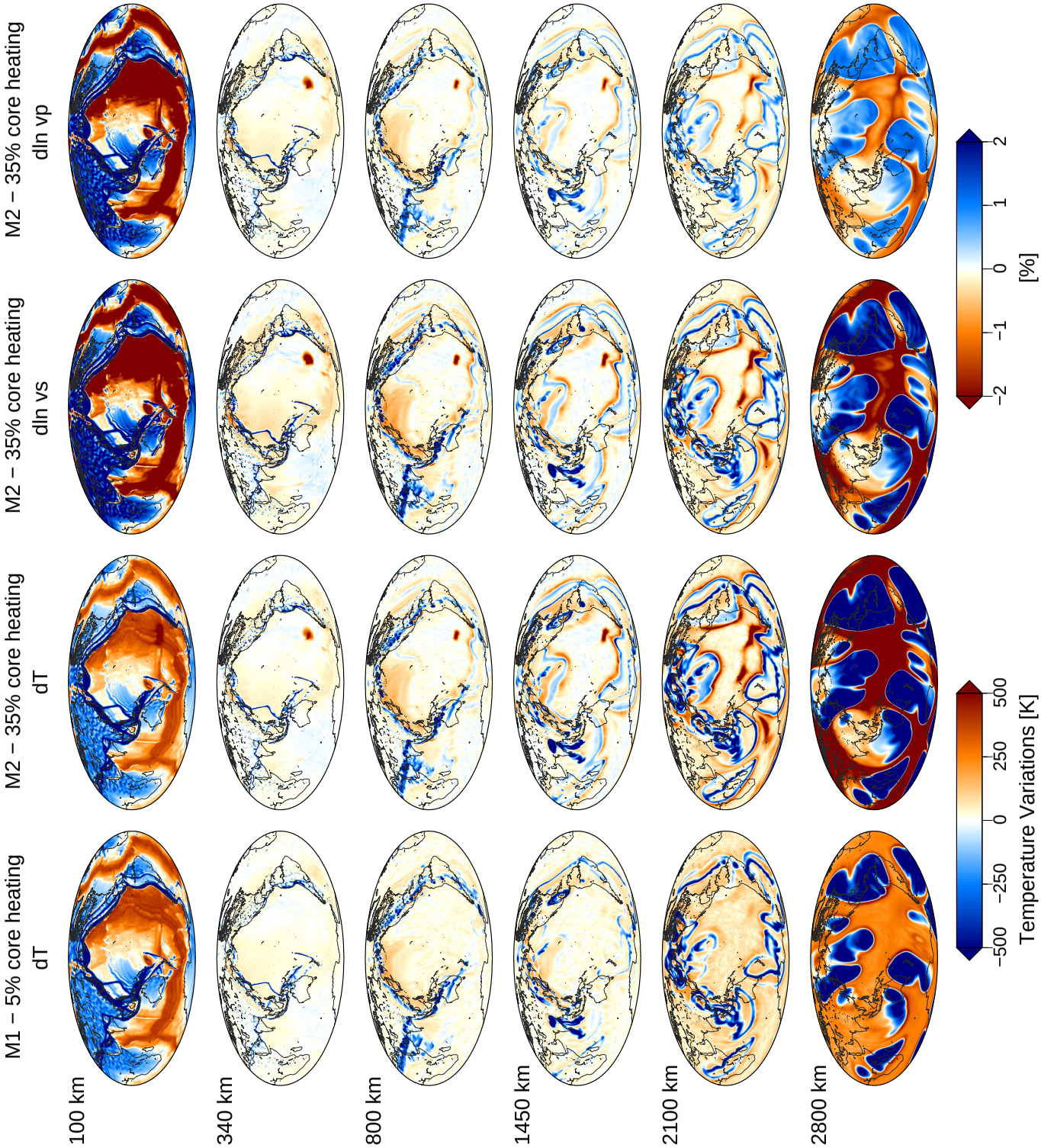

Figure 3. Depth slices through mantle circulation models M1 and M2 with weak and strong core heat flux, respectively. (left) Temperature variations in M1 and M2 and (right) elastic structure in M2 (strong core heating) for variations of shear, as well as compressional wave velocity relative to their radial average. Absolute values of seismic velocities are obtained from absolute values of temperature using the mineralogical model SLB [*Stixrude and Lithgow-Bertelloni*, 2005, 2007].

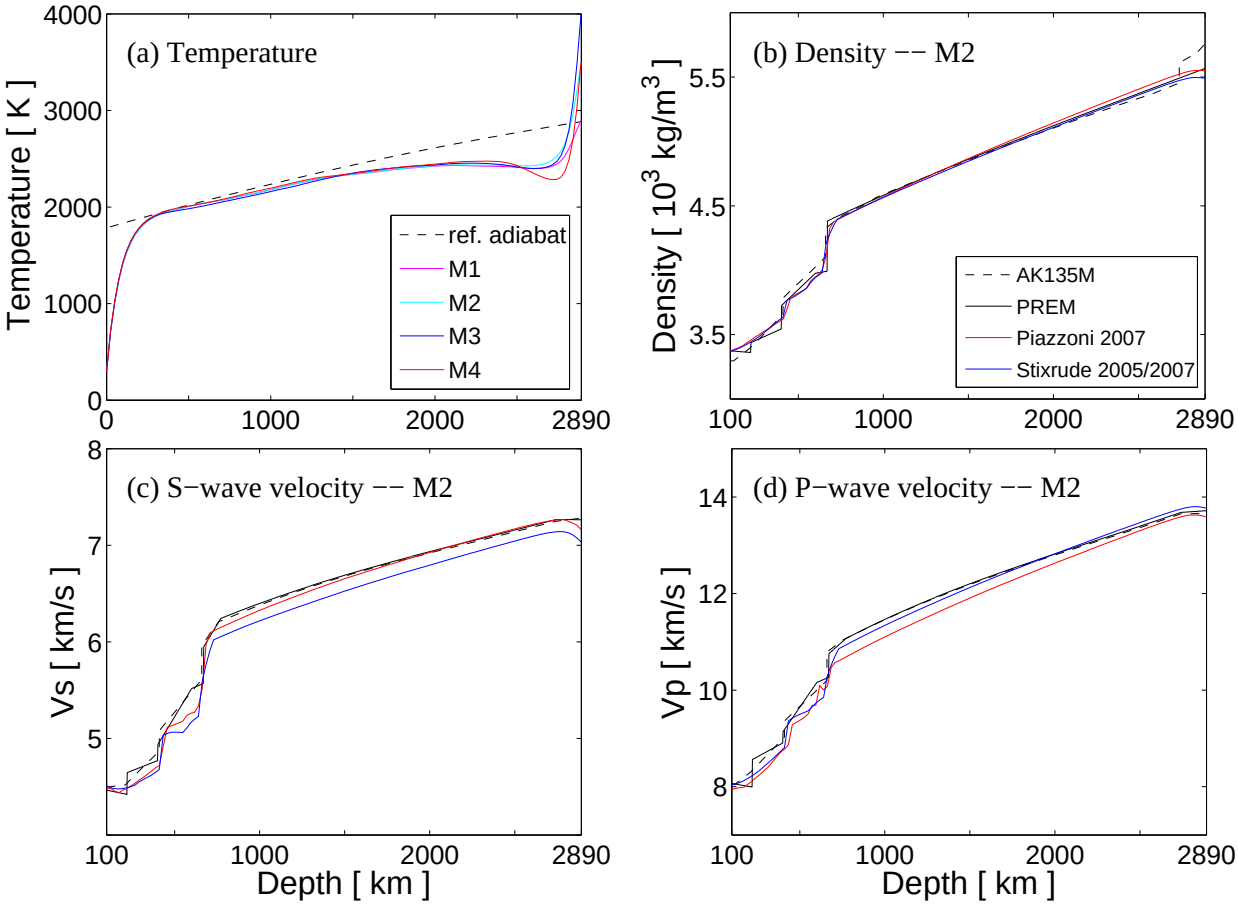

Figure 4. a) Temperature profiles of models M1–M4 together with the reference adiabat used in the simulations. Note that all profiles are subadiabatic due to internal heating and depart by about 300–500 K from the adiabat in the lowermost mantle. b) Laterally averaged profiles of density derived from model M2 using the mineralogical models PSBD [*Piazzoni et al.*, 2007] and SLB [*Stixrude and Lithgow-Bertelloni*, 2005, 2007] for conversion of temperature to density. Density of the seismic reference models AK135M and PREM are shown for comparison. c) and d) same as b) for averaged 1-D profiles of shear and compressional wave velocities obtained from model M2, respectively.

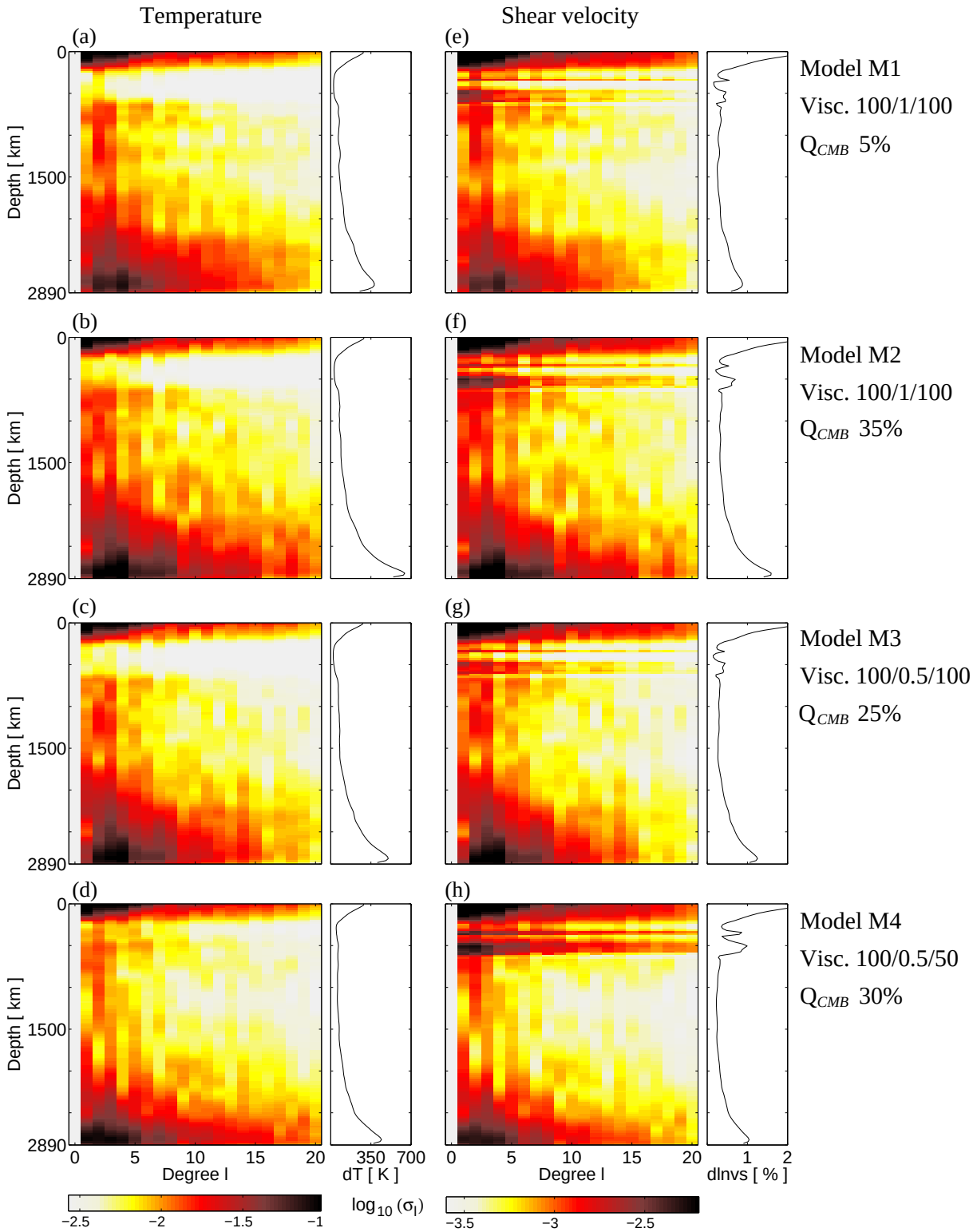

Figure 5. Spectral power of heterogeneity in (a–d) temperature and (e–h) shear wave velocity for mantle circulation models M1–M4 (see text). Spectral power is plotted on a logarithmic scale as a function of spherical harmonics degree and depth. Subplots on the right of each spectral heterogeneity map show the root-mean-square amplitudes of temperature and v_s perturbations as a function of depth, respectively. Relative variations of shear wave velocity are derived from the mantle circulation models using the mineralogical model SLB [*Stixrude and Lithgow-Bertelloni*, 2005, 2007]. Note the differences between thermal and seismic heterogeneity. For example, the change in spectral power from the upper to the lower mantle is of opposite sense. The narrow bands of strong power in v_s in the upper mantle are a consequence of the mineralogy in the transition zone (see text), even though there is reduced thermal heterogeneity in these depth levels. Note the overall increase in spectral amplitude of temperature and v_s in the lowermost mantle.

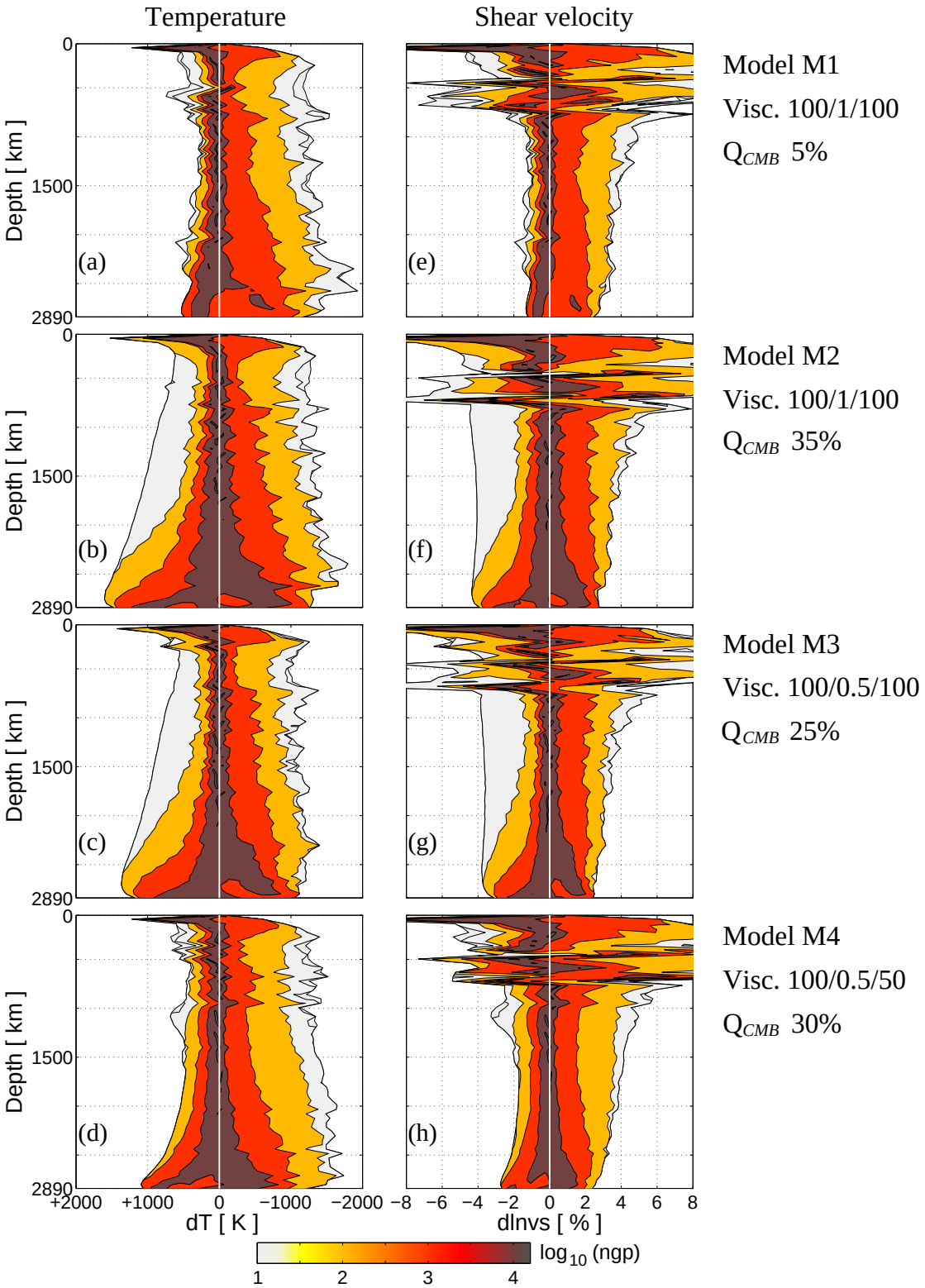

Figure 6. (a–d) Histograms of temperature variations in mantle circulation models M1–M4. Color scale and contours represent number of grid points (*ngp*) on a logarithmic scale as a function of temperature perturbation and depth. Contour lines are plotted for $log_{10}(ngp) = 1, 2, 3$ and 4. Note: The x axis (dT) of the temperature histograms has been flipped in consequence of the negative sensitivity of v_s to temperature to ease the comparison with the histograms for v_s. (e–h) Same as (a–d) for variations of shear wave velocity obtained from mantle circulation models M1–M4 using the mineralogical model SLB [*Stixrude and Lithgow-Bertelloni*, 2005, 2007]. Comparison of thermal and elastic structures reveals the general decrease in sensitivity of v_s to temperature with depth. Maximum thermal variations on the order of −1000 K from cold slabs and more than +1000 K from hot upwellings in the lowermost mantle (M2–M4) result in maximum v_s anomalies of +2% and −4%. In contrast to these models with strong core heating, model M1 has much lower negative v_s amplitudes of around −1% resulting from positive thermal anomalies of only up to +500 K.

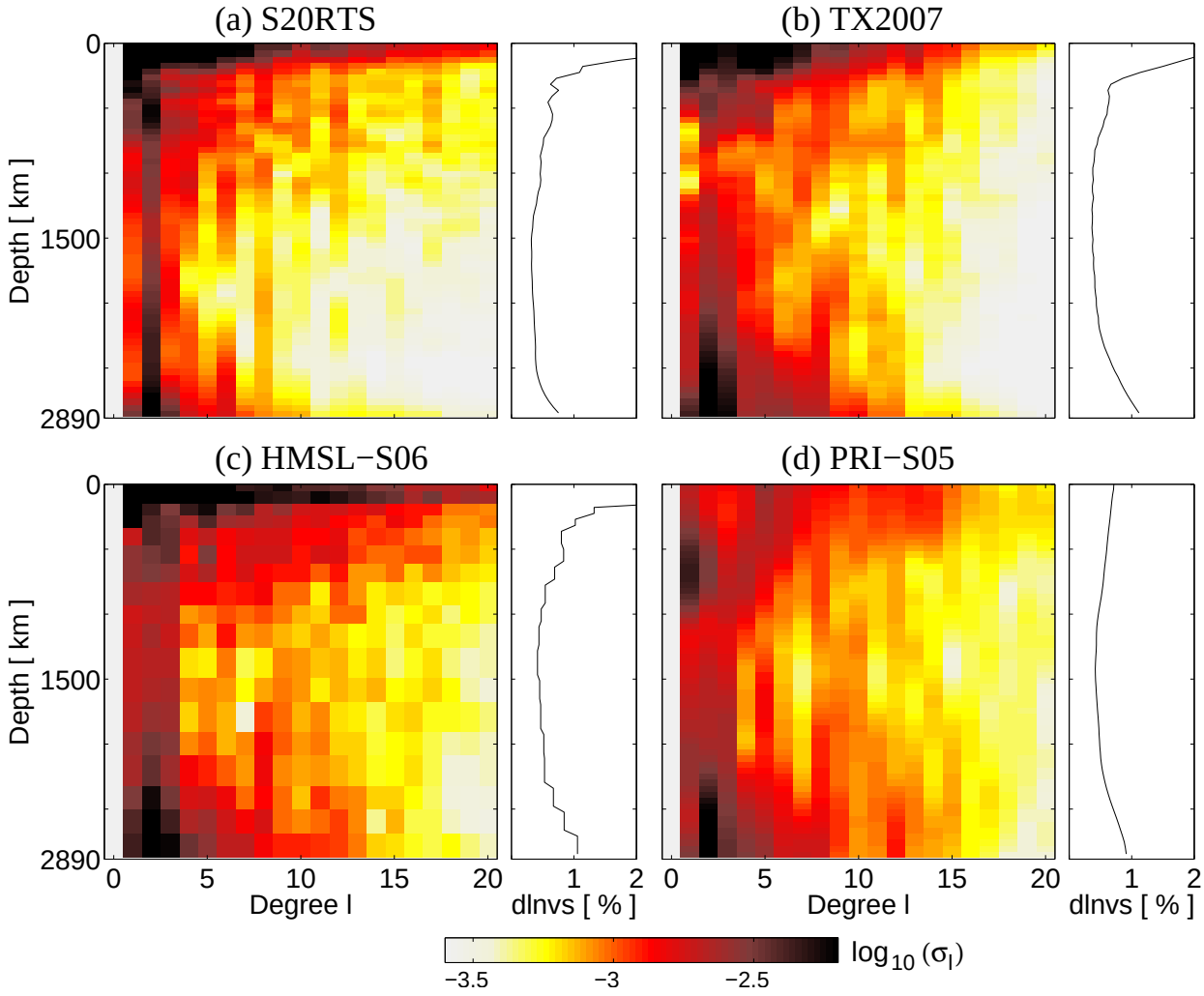

Figure 7. Spectral power of heterogeneity in tomographic S wave models S20RTS [*Ritsema et al.*, 2004], TX2007 [*Simmons et al.*, 2007], HMSL-S06 [*Houser et al.*, 2008] and PRI-S05 [*Montelli et al.*, 2006] plotted on a logarithmic scale as a function of spherical harmonics degree and depth. Subplots on the right of each spectral heterogeneity map show the root-mean-square amplitudes of relative v_s perturbations in each depth.

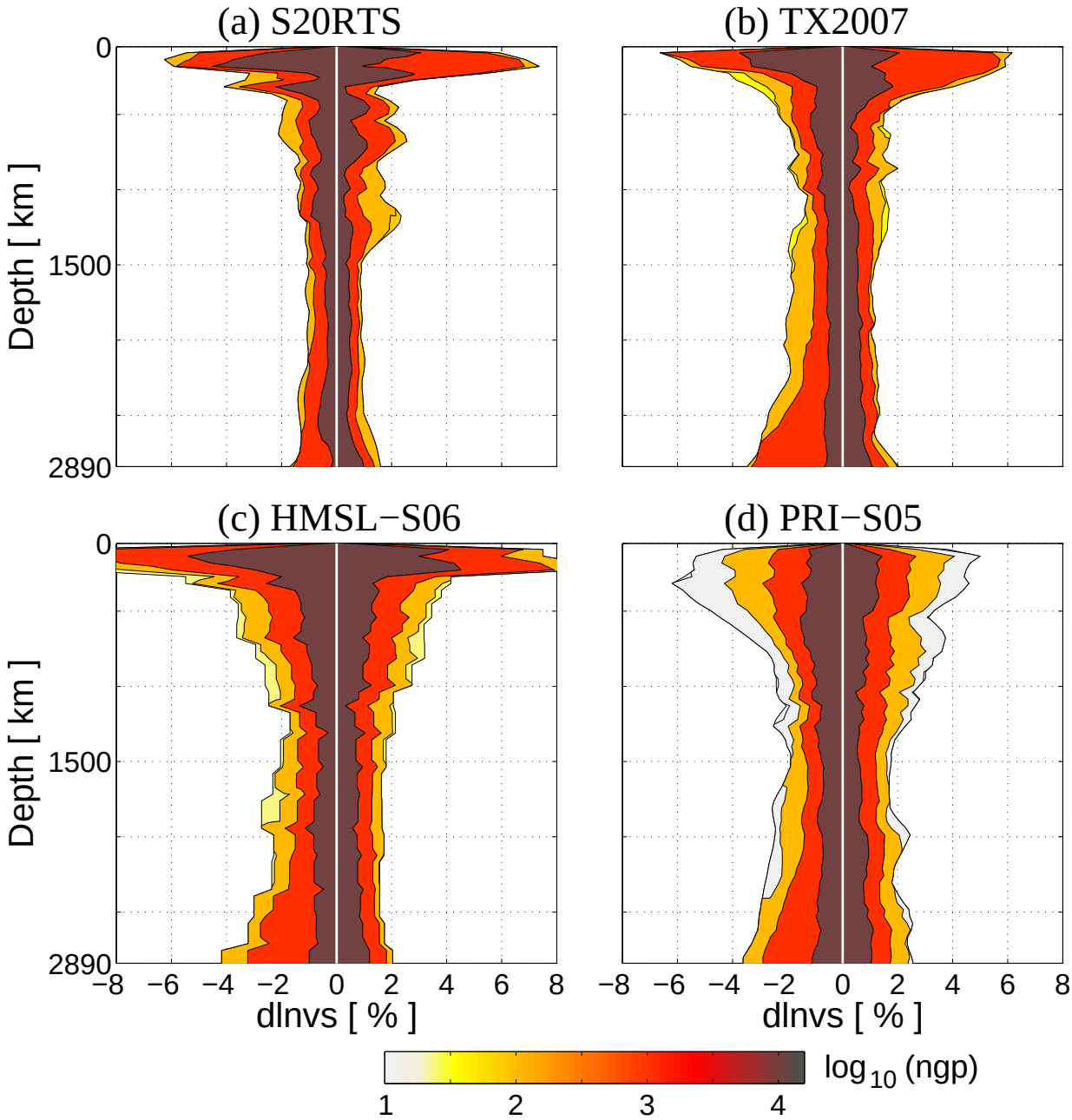

Figure 8. Histograms of relative variations of shear wave velocity in tomographic models S20RTS [*Ritsema et al.*, 2004], TX2007 [*Simmons et al.*, 2007], HMSL-S06 [*Houser et al.*, 2008] and PRI-S05 [*Montelli et al.*, 2006]. Color scale and contour lines are the same as in Figure 6. The tomographic histograms are normalized to the number of grid points in our MCMs to allow for a direct comparison with Figure 6.

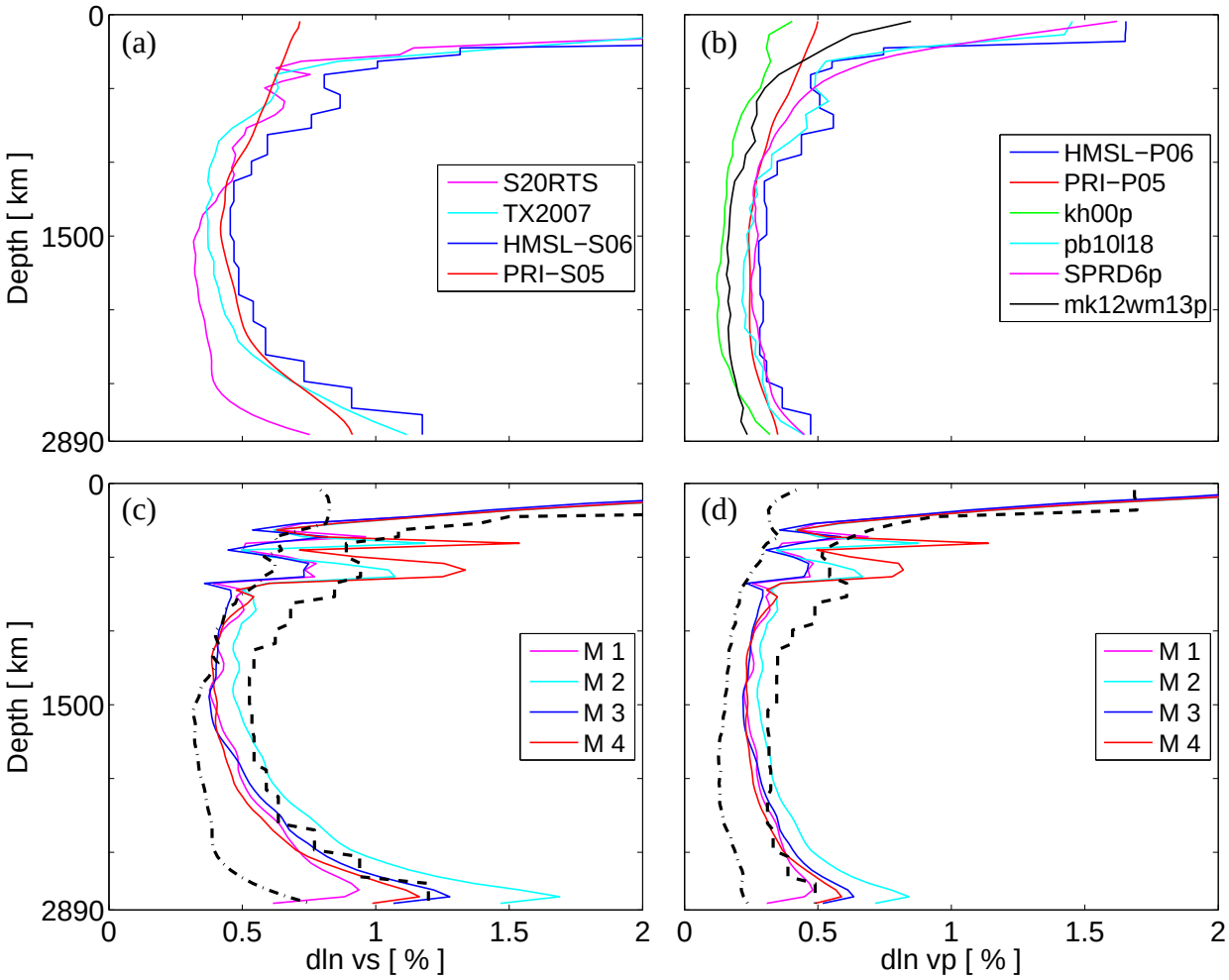

Figure 9. Comparison of root-mean-square amplitudes of heterogeneity between tomographic and geodynamic models. a) RMS profiles of variations in S-wave velocity of tomographic models S20RTS [*Ritsema et al.*, 2004], TX2007 [*Simmons et al.*, 2007], HMSL-S06 [*Houser et al.*, 2008] and PRI-S05 [*Montelli et al.*, 2006]. b) RMS profiles of P-wave velocity of models HMSL-P06 [*Houser et al.*, 2008], PRI-P05 [*Montelli et al.*, 2006], kh00p [*Kárason and van der Hilst*, 2001], pb10l18 [*Masters et al.*, 2000], SPRD6p [*Ishii and Tromp*, 2001] and mk12wm13p [*Su and Dziewonski*, 1997]. a) and b) illustrate the variation among different tomographic models but also show a general increase in heterogeneity with depth in the lower mantle. c) RMS profiles of S-wave heterogeneity predicted from models M1–M4 using the mineralogical model SLB [*Stixrude and Lithgow-Bertelloni*, 2005, 2007]. Dashed and dash-dotted black lines show upper and lower bounds of tomographic heterogeneity strength taken from a). d) same as c) but for P-wave heterogeneity with dashed and dash-dotted black lines corresponding to upper and lower bounds of the P-wave models in b). Note that the amplitudes of heterogeneity derived from the geodynamic models falls within the bounds of tomographic models.

Table 1. Physical parameters and values employed in the simulations of mantle circulation. Values in this table were kept constant in all four mantle circulation models M1–M4.

outer shell radius	6370	km
inner shell radius	3480	km
$T_{Surface}$	300	K
η_{ref} (reference viscosity)	1.0×10^{21}	Pa s
thermal conductivity k	3.0	$\mathrm{W\,m^{-1}\,K^{-1}}$
thermal expansivity α (surface)	4.011×10^{-5}	$\mathrm{K^{-1}}$
thermal expansivity α (CMB)	1.256×10^{-5}	$\mathrm{K^{-1}}$
internal heating rate Q_{int}	6.0×10^{-12}	$\mathrm{W\,kg^{-1}}$
heat capacity	1.134×10^{3}	$\mathrm{J\,kg^{-1}\,K^{-1}}$
Ra_H (based on η upper mantle)	$\simeq 10^{9}$	

Table 2. Variable parameters and respective values in models M1–M4. Viscosities in the lithosphere (LI), upper mantle (UM) and lower mantle (LM) are indexed to the reference viscosity of $\eta_{ref} = 1 \times 10^{21}$ Pa s.

Model	Viscosity structure LI/UM/LM w.r.t η_{ref}			Depth of UM/LM boundary [km]	T_{CMB} [K]	CMB heat flow [TW]	(% of surface heat flow)
M 1	100	1	100	660	2900	1.5	(5)
M 2	100	1	100	660	4200	12	(35)
M 3	100	0.5	100	660	4000	9	(25)
M 4	100	0.5	50	450	3500	10	(30)